Ubiquitous Sea Surface Temperature Anomalies Increase Spatial Heterogeneity of Trade Wind Cloudiness on Daily Time Scale

XUANYU CHEN,[a,b] JULIANA DIAS,[b] BRANDON WOLDING,[a,b] ROBERT PINCUS,[c] CHARLOTTE DEMOTT,[d] GARY WICK,[b] ELIZABETH J. THOMPSON,[b] AND CHRIS W. FAIRALL[b]

[a] *Cooperative Institute for Research in Environmental Sciences, University of Colorado Boulder, Boulder, Colorado*
[b] *NOAA/Physical Sciences Laboratory, Boulder, Colorado*
[c] *Lamont-Doherty Earth Observatory, Columbia University, Palisades, New York*
[d] *Department of Atmospheric Science, Colorado State University, Fort Collins, Colorado*

(Manuscript received 21 April 2023, in final form 3 October 2023, accepted 5 October 2023)

ABSTRACT: The impact of weak submeso- to mesoscale SST anomalies on daily averaged trade cumulus cloudiness is investigated using satellite observations that have been validated against shipboard measurements from the Atlantic Tradewind Ocean–Atmosphere Mesoscale Interaction Campaign (ATOMIC). Daily spatial SST anomalies are identified from GOES–POES Blended SST analysis within a 10° × 10° region during January and February 2020. Daily averaged cloud fraction and 10-m neutral wind from satellite observations and reanalysis are composited over the identified SST features, using a common coordinate system based on the near-surface background wind directions. Composites of satellite cloud fraction show a statistically significant increase of cloudiness over the SST warm core with a reduction of cloudiness away from it. These responses are largely the same but with opposite signs over SST cold anomalies, suggesting that spatial heterogeneity in SST can locally imprint on daily cloud fraction. Composites of daily 10-m wind speed and wind convergence anomalies from both satellite and reanalysis show that surface wind speed is increased over SST warm anomalies, implying enhanced turbulence over warmer SSTs. Correspondingly, the surface convergence anomalies in these composites are located around the maximum downwind SST gradient, offset downwind from the cloudiness anomalies. These results indicate that the response of daily cloudiness to these SST anomalies is more likely generated by spatial variability of surface-driven turbulence and surface fluxes rather than that of surface or boundary layer convergence.

KEYWORDS: Mesoscale processes; Boundary layer; Cumulus clouds; Air-sea interaction

1. Introduction

Marine trade cumuli play a key role in Earth's climate by cooling the planet. Understanding the key factors that control the trade cumulus cloud amount at cloud base has become an active topic of investigation in recent years (Vial et al. 2017). Cloud-base cloudiness is controlled by the local interplay between turbulent, convective, and radiative processes, each of which can further interact with their surrounding environment and can be influenced by shallow mesoscale cloud organization (Vial et al. 2017; Bony et al. 2017; Schulz et al. 2021). Studies have evaluated effects of large-scale cloud-controlling factors, including near-surface wind speed, lower-tropospheric stability, free-troposphere relative humidity, subsidence, and sea surface temperature (SST), on low-level cloud cover and trade cumulus organizations (e.g., McCoy et al. 2017; Bony et al. 2020; Scott et al. 2020; McCoy et al. 2023). Since shallow cumuli are rooted in the subcloud mixed layer (Malkus 1958; Johnson and Ciesielski 2017), where the atmosphere can be forced by mesoscale ocean processes (Small et al. 2008; Seo et al. 2023), in this study we investigate the role of mesoscale and/or submesoscale SST anomalies in locally regulating trade-cumulus cloudiness.

Our study region is the northwestern tropical Atlantic, where in situ measurements were recently collected as part of the Elucidating the role of cloud-circulation coupling in climate (EUREC^{4}A) field campaign (Bony et al. 2017; Stevens et al. 2021) and Atlantic Tradewind Ocean–Atmosphere Mesoscale Interaction Campaign (ATOMIC) from 9 January to 11 February 2020 (Quinn et al. 2021). The EUREC^{4}A/ATOMIC sampling region is about 250 nautical miles (nm; ~465 km) upwind of Barbados, which, at this time of year, has fewer ocean eddies and less persistent SST fronts as compared to the nearby coastal western boundary current region (Fig. 1 of Mauzole 2022). Nevertheless, mesoscale to submesoscale SST spatial anomalies still exist ubiquitously in daily satellite SST analysis in the EUREC^{4}A/ATOMIC area, albeit with a weak magnitude compared to the coastal North Brazil Current (NBC) rings (Fratantoni and Glickson 2002). In situ SST measurements from wave gliders in this wintertime ATOMIC campaign estimated SST variability up to 0.7°C across an order of 10–100 km with a maximum gradient of (0.047°C km^{-1}) (Iyer et al. 2022a). Similar SST variability was also observed on board NOAA ship *Ronald H. Brown* in ATOMIC (Fig. 1). These ocean submesoscale gradients of SST exist in this region due to nearby eddies, fronts, and filaments of different water properties (temperature, salinity, currents; Fratantoni and Glickson 2002; Fratantoni and Richardson 2006; Iyer et al. 2022a,b).

Clouds have been shown to respond to SST features in various ways and in a variety of ocean regions. In the tropical

Corresponding author: Xuanyu Chen, xuanyu.chen@colorado.edu

DOI: 10.1175/JAS-D-23-0075.1

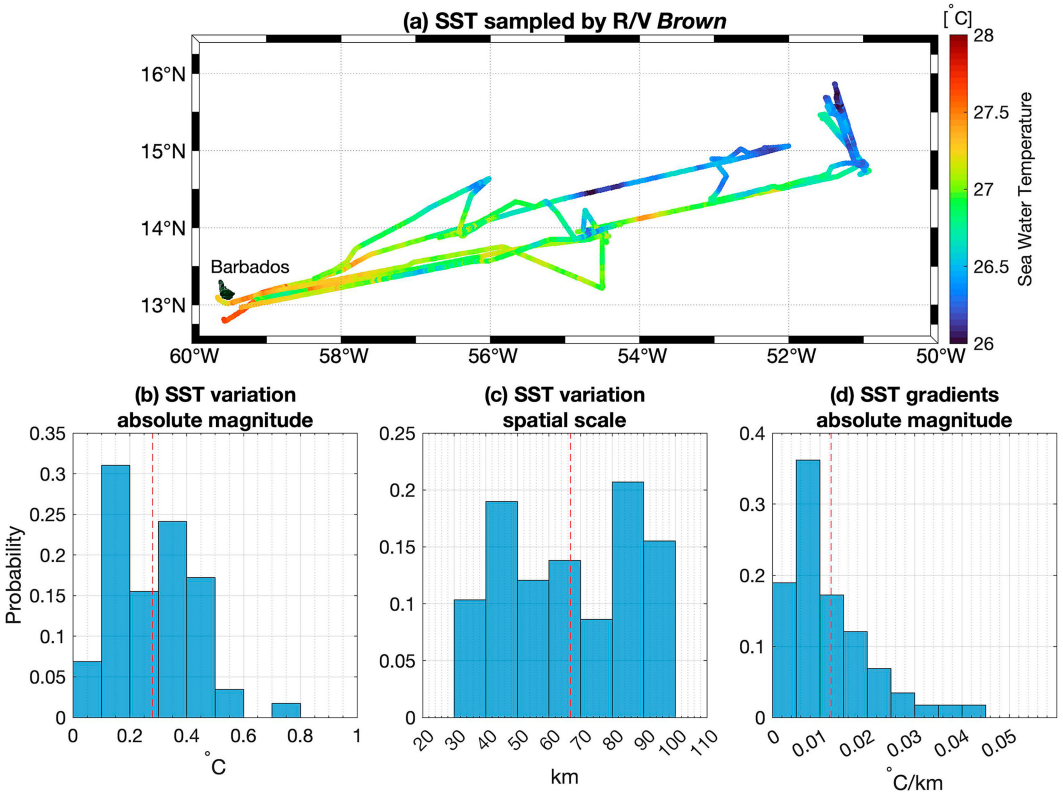

FIG. 1. (a) Map of SST sampled by R/V *Brown* (at 5-cm depth) during the ATOMIC campaign period. (b)–(e) Histograms of (b) SST variation magnitude, (c) variation length scale, and (d) the associate SST spatial gradients sampled on days with SST variance in the upper quartile and when R/V *Brown* is in transit. The vertical red dashed line in each panel represents the mean value. Details of the characteristics estimations are included in appendix A.

western Pacific warm pool, a 1-day lag correlation exists between the SST Laplacian and rainfall (Li and Carbone 2012), which may be related to enhanced cloudiness over mesoscale SST warm patches (Skyllingstad et al. 2019). Enhanced cloudiness is evident above large-scale SST features like the Gulf Stream (Minobe et al. 2008). Similar cloud response appears even at smaller spatial scales near large warm-to-cold SST gradients, as seen in the Mediterranean Sea (Desbiolles et al. 2021), at the downwind edge of midlatitude mesoscale warm-core rings (Park et al. 2006), and downwind of 10-km warm spots in the western Caribbean Sea (Malkus 1957).

In all of the above studies, increased cloudiness is connected to vertical motion triggered by SST-induced surface wind convergence, which can be generated via two primary mechanisms. In one mechanism, the boundary layer air temperature and air density are affected by local SST perturbations, resulting in pressure adjustment (Lindzen and Nigam 1987) due to reduced hydrostatic pressure over warm water and increased hydrostatic pressure over cold water (Shimada and Minobe 2011; O'Neill et al. 2010b). When the associated horizontal hydrostatic pressure gradients dominate the momentum budget, the wind convergence is highly correlated with the negative SST Laplacian (e.g., Shimada and Minobe 2011; Lambaerts et al. 2013; Foussard et al. 2019). In the other mechanism, turbulence is enhanced over warmer SST, helping to redistribute the larger horizontal momentum in the upper-atmospheric boundary layer to the surface (e.g., Hayes et al. 1989; Shimada and Minobe 2011; O'Neill et al. 2010b). This downward momentum mixing mechanism (Wallace et al. 1989; Hayes et al. 1989) is associated with acceleration of surface wind over warmer SST and surface wind convergence near the maximum SST gradient (e.g., Chelton et al. 2001; O'Neill et al. 2003; Chelton et al. 2004; O'Neill et al. 2005; Small et al. 2008; O'Neill et al. 2010a; Meroni et al. 2020). As a result, the wind divergence pattern mirrors the SST gradient dipole over semicircular ocean eddies (e.g., Park et al. 2006; Frenger et al. 2013; Byrne et al. 2015; Foussard et al. 2019). The dominant mechanism of surface wind response to SST spatial variations further depends on large-scale advection (Schneider and Qiu 2015; Skyllingstad et al. 2019; Foussard et al. 2019) and the spatial scale of the SST anomalies (Spall 2007). These two mechanisms in changing surface momentum are nonexclusive and can act in concert (O'Neill et al. 2010b; Foussard et al. 2019).

Surface wind convergence is not the only pathway for clouds to be impacted by spatial SST anomalies. Over Southern Ocean warm-core eddies, enhanced (or reduced) cloudiness and rain were found to be offset from the surface convergence (or divergence) center in both satellite observations (Frenger et al. 2013) and numerical simulations (Byrne et al. 2015). This

suggests that cloudiness is modulated by changes of boundary layer turbulence and convective mixing over SST anomalies (Frenger et al. 2013; Byrne et al. 2015). Recent in situ measurements support this view. Daytime warming of SST over large areas of the ocean is shown to drive surface-based convective turbulence in the atmospheric boundary layer (de Szoeke et al. 2021), increasing atmospheric mixed-layer height and allowing for more cumulus cloud formation in the equatorial Indian Ocean (de Szoeke et al. 2021; Johnson and Ciesielski 2017). Convergence was not found in these two prior studies. Similarly, a reduction of cloudiness over an SST cold patch south of the ATOMIC region was linked to reduced turbulence overhead, not coincident with surface convergence (Acquistapace et al. 2022). Hence, these studies show consensus that boundary layer turbulence from surface buoyancy fluxes and/or wind shear can increase cumulus cloudiness by increasing the opportunity for boundary layer thermals to reach their lifting condensation levels (Johnson and Ciesielski 2017).

Intriguingly, the locally increased SSTs associated with mesoscale (or finer) SST warm patches seem to have an opposite effect on cloudiness compared to a uniform surface warming, which is often prescribed in idealized climate studies (e.g., Rieck et al. 2012; Bretherton and Blossey 2014; Klein et al. 2017). Specifically for trade cumulus clouds, idealized LES results show that a spatially uniform increase in SST leads to enhanced surface fluxes and cloud deepening (Rieck et al. 2012). The associated entrainment of warmer and drier air from above the trade inversion then warms and dries both the cloud and subcloud layer, resulting in reduced cloud cover. This surface-flux desiccation mechanism proposed by Rieck et al. (2012) can also be considered as a form of entrainment liquid flux adjustment, a thermodynamic mechanism conceptualized to explain stratocumulus thinning in a warmer climate (Bretherton and Blossey 2014). Both of these mechanisms reflect the thermodynamic control on shallow cumulus cloudiness through humidity (Vogel et al. 2022). However, a recent analysis of observational data from EUREC^{4}A presents evidence that lower-tropospheric convective mixing dominates the thermodynamic control and dynamically increases trade cumulus cloudiness (Vogel et al. 2022).

How trade cumulus cloudiness might respond to the relatively weak but ubiquitous SST anomalies in the EUREC^{4}A/ATOMIC region begs further investigation. To complement the cold ocean eddy case study from EUREC^{4}A-Ocean campaign (Acquistapace et al. 2022), our study aims to provide characterization of trade cumulus responses to SST anomalies in the ATOMIC region as well as to better understand the processes involved. Our approach also serves as a benchmark for assessing the ability of GCMs and LES in representing mesoscale air–sea interactions in the trade wind regime.

Relevant data and the compositing method are described in sections 2 and 3, respectively. In section 4, we show assessments of satellite observations, characteristics of SST anomalies in the study region, and the cloud and wind anomalies associated with SST features. In section 5, the potential mechanisms linking SST, winds, and clouds are discussed. Section 6 provides a summary of the key findings and their implications for future studies.

2. Data

Our data analysis is constrained spatially in a 10° × 10° region (8°–18°N, 58°–48°W) and temporally from 1 January to 24 February 2020. The location and time period are purposefully chosen to encompass in situ measurements collected on R/V *Brown* (Quinn et al. 2021) and to be the same as the satellite SST assessment period in Wick et al. (2023).

a. *In situ measurements from R/V* Brown

As part of ATOMIC, R/V *Brown* conducted in situ and remote sensing measurements of oceanic and atmospheric properties from 7 January to 13 February 2020 (Quinn et al. 2021). For validation purposes, we use the 10-min-averaged seawater temperature measured from the sea snake instrument operating at 5-cm depth (Thompson et al. 2021b) and the hourly temporal cloud fraction derived from ceilometer measurements (Thompson et al. 2021a). Note that the hourly cloud fraction describes the frequency of cloud detection within an hour irrespective of the height of the cloud.

b. *Satellite retrievals and analysis products*

To identify SST anomalies, we primarily use the NOAA 0.05°, daily Geostationary Operational Environmental Satellite–Polar Orbiting Environmental Satellite (GOES–POES) Blended analysis (GPB hereafter; Maturi et al. 2017). Additional sensitivity tests are conducted with the Met Office Operational Sea Surface Temperature and Sea Ice Analysis (OSTIA hereafter; Good et al. 2020) (see appendix C). Our results are not sensitive to this choice of SST analysis product.

Although these two level-4 (L4) gridded SST products have skills representing the SST variability at spatial scale larger than 0.5°–1°, they cannot fully produce the in situ submesoscale SST variability (Wick et al. 2023). As a result, for direct comparison with R/V *Brown* in situ measurements, we use the version 2.7 of the 0.02°, hourly level-3 collated *GOES-16* SST retrieval data (G16-L3C SST hereafter; Petrenko et al. 2019), which is also one geostationary SST input that the GPB analysis ingested but was not used by OSTIA (see Table 1 of Wick et al. 2023). This G16-L3C SST data is not chosen to identify SST anomalies because the presence of clouds prevents the retrieval of SST with infrared sensors, and hence, the high-resolution retrievals are limited to clear-sky conditions. For this reason, making use of the L3C SST retrievals is not straightforward and will require a declouding algorithm (e.g., Park et al. 2006).

The L4 SST products have the advantage of providing gap-free and spatially continuous SST values, which represent the daily foundation temperature free of diurnal influence. Moreover, because of the small diurnal SST variations throughout the EUREC^{4}A/ATOMIC region, we can further regard the L4 daily SST maps as a good estimate of the daily mean SST fields. Therefore, our choice here means that we set out to estimate the daily averaged location of SST anomalies in the EUREC^{4}A/ATOMIC region.

We calculate the daily averaged cloud area fraction on the 0.25° × 0.25° ERA5 grid from the 0.02°, hourly cloud mask inherent in the G16-L3C SST data, which is generated by the Advanced Clear-Sky Processor for Oceans (ACSPO) (referred to as G16-L3C ACSPO cloud mask hereafter). In this cloud mask, misclassifications of clear pixels as cloudy and false cloud detections over ocean thermal fronts have been minimized (Petrenko et al. 2010). Note that the G16-L3C ACSPO cloud mask likely shares the same limitations with the NOAA Enterprise Cloud Mask in the *GOES-16* satellite (Heidinger and Straka 2020), where shallow clouds with cloud top below 2 km are the most commonly missed cloud type (Luebke et al. 2022). At a given hour, it is unlikely for trade cumuli to completely cover a 10° × 10° area. However, because the clear-sky identification is affected by clouds at different altitudes and can be affected by other cloud-equivalent factors, there are times (~1%) when the clear-sky mask suggests our study region being 100% cloudy, which we exclude to reduce cloudiness signal coming from factors other than trade cumuli. Note that the results are insensitive to including these data.

We use the 0.25°, 6-hourly Near-Real Time Cross-Calibrated Multi-Platform ocean surface vector wind analysis (CCMP-NRT hereafter; Mears et al. 2019) to estimate the daily averaged 10-m neutral wind and its divergence field. For the data period examined here, CCMP-NRT takes in vector wind retrieval only from the Advanced Scatterometer (ASCAT). In areas without ASCAT coverage, wind fields are estimated with the variational analysis method (Atlas et al. 2011), where NCEP GDAS wind fields are used as a first guess and the final wind fields are optimized based on available radiometer wind speed retrievals. Note that ASCAT retrieved winds are much less contaminated by rain compared to previous Ku-band scatterometers (e.g., QuikSCAT) and have been recently used to study changes of surface wind divergence associated with mesoscale convective systems (King et al. 2022).

c. ERA5

ERA5, the fifth generation of atmospheric reanalysis produced by the European Centre for Medium-Range Weather Forecasts (ECMWF; Hersbach et al. 2020), is utilized to compare with satellite analysis and to aid interpretation of the satellite composites. ERA5 uses the daily OSTIA SST analysis as the ocean surface boundary condition and provides hourly atmospheric fields at horizontal resolutions of 0.25°. Its 10-m surface wind field is close to the ASCAT observations (Belmonte Rivas and Stoffelen 2019). Above 150 m, the ERA5 wind biases are recently evaluated against EUREC^{4}A soundings in Savazzi et al. (2022). In our analysis, 10-m neutral wind field and total cloud cover are taken at the same temporal frequency as their satellite counterparts (6 hourly and hourly, respectively) to compute the daily averaged fields. Ten-meter surface wind convergence is computed using central differences.

3. Methods

We apply feature-based composite analysis to detect daily atmospheric response, represented as spatial anomalies, over SST features. A key step is to identify daily SST anomalies and locate their edges, which provide the locations to construct composites.

a. Definition of spatial anomalies

As in previous studies (e.g., O'Neill et al. 2003), we define spatial anomalies in the daily SST and atmospheric fields as spatial high-pass filtered signals using the following high-pass response function:

$$\mathcal{R}_{\mathrm{hp}}(k_x, k_y) = 1 - e^{-2(k_x^2+k_y^2)/k_c^2},$$

where k_x and k_y are the wavenumbers in longitudinal and latitudinal directions, respectively, and $k_c = 2\pi/L_c$ is the characteristic wavenumber corresponding to a 300-km characteristic length scale L_c.

For data in a limited two-dimensional (2D) area, high-pass spectral filtering can generate high-wavenumber spectral artifacts, which we aim to reduce by adopting the following procedures (Kruse and Smith 2015). First, the given 2D data field $A(x, y)$ is deplaned by subtracting a least squares best-fit plane from the original data field. Then, the anomaly field A' is obtained by applying a high-pass filter to the deplaned perturbation field using a 300 km characteristic length scale (L_c). Note that this characteristic length scale is consistent with the pressure adjustment length scale estimated using U/f (Spall 2007) and that the results remain qualitatively similar when L_c varies between 200 and 400 km. The associated large-scale background field is by definition $A_{\mathrm{bg}} = A - A'$. To further limit possible contamination from edge artifacts near the boundary of our study region, we extend the edge of our data region by 2° for the above procedures, which is large enough ($>0.55L_c$) so that edge artifact amplitude becomes negligible within our study region (Kruse and Smith 2015).

b. Detection of SST anomaly features

We detect coherent SST objects from GPB L4 SST observations. Spatially coherent warm and cold anomalies are identified as contiguous regions of anomalous SST that exceed an absolute anomaly of 0.1°C based on an 8-connectivity criterion (Dias et al. 2012). We only select features that are larger than 5 × 5 GPB SST pixels (one ERA5 grid box) and whose centroids are within the region of study. An example of the detection results is shown in Fig. 2.

Submesoscale-to-mesoscale SST anomalies are ubiquitous in the ATOMIC region with 1156 warm anomalies and 1052 cold anomalies detected in the domain and time period considered. Properties of these SST objects are also computed by the algorithm. Specifically, the object's centroid, area equivalent radius (R_e), major (L_{maj}) and minor axis lengths, orientation angle, and bounding box are relevant for constructing composites and computing the large-scale background mean.

c. Construction of feature-based composites

We adopt a normalized coordinate system to composite atmospheric fields over the irregular and elongated SST features. The method, originally developed for Gulf Stream rings

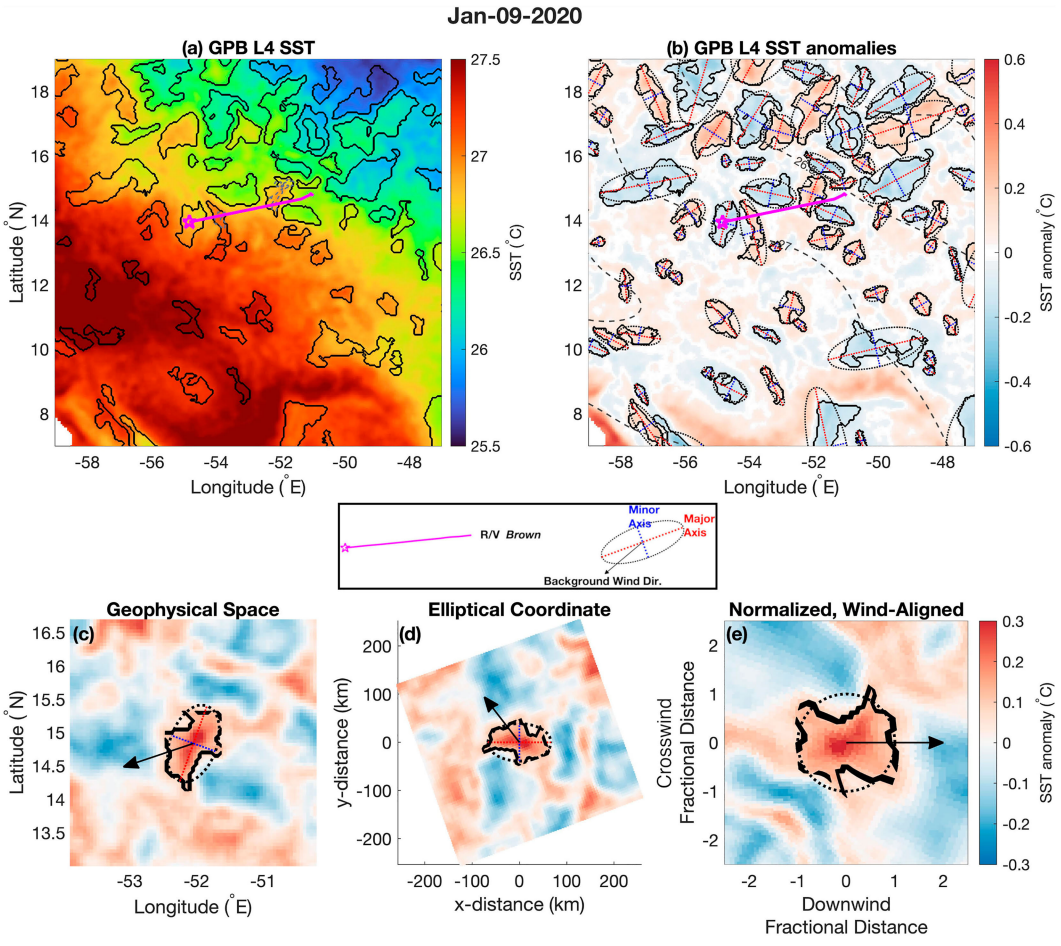

FIG. 2. Examples of (a) daily SST fields from GPB, (b) SST anomalies identified with the object-based algorithm and (c)–(e) coordinate transformation for composite analysis. In all panels, black solid contours outline the boundary of SST anomaly objects. In (a), the magenta solid line represents the R/V *Brown* ship track between 9 and 10 Jan 2020 (UTC) with the starting location marked by a magenta star; gray dashed contours within two SST anomalies crossed by R/V *Brown* are the estimated locations of subdaily SST anomalies in G16-L3C SST retrievals. In (b), large-scale background SST is denoted with black dashed lines with a 0.5°C increment. Each SST anomaly object is approximated by an ellipse (thin black dotted line) with major (red dotted line) and minor axis (blue dotted line). In (c)–(e), the black vector denotes the averaged large-scale background wind direction within the data cutout. Black dotted circle in (e) outlines the normalized ellipse boundary.

(Park et al. 2006), defines the coordinate based on background wind direction, which is a common choice as it physically describes the SST gradient magnitude experienced by the background wind. The coordinate transformation involves three key steps illustrated in Figs. 2c–e (see appendix B for mathematical details).

For each SST feature, a given geophysical data field (e.g., SST anomalies, cloud fraction anomalies) is first extracted in a $3L_{\text{maj}} \times 3L_{\text{maj}}$ square area centered at the SST object centroid (Fig. 2c). This is referred to as a data cutout, whose geophysical coordinate is converted to a feature-centric Cartesian distance coordinate. Next, each SST feature is approximated by an ellipse using the object's major and minor axis (e.g., Fig. 2b), and a new distance coordinate is formed using the feature's major axis as its abscissa (Fig. 2d). The final SST feature-centric, normalized, and background wind-aligned coordinate system (Fig. 2e) is constructed by normalizing the data position in this new distance coordinate with the elliptical radii and aligning the abscissa with the averaged 10-m large-scale background wind. Note that the mean large-scale background wind is computed over the data cutout area using the CCMP wind field and that the composite results are not sensitive to using the ERA5 counterpart. Additionally, a shared grid representing fractional distance from −3 to 3 with a 0.05 spacing is set up in this final coordinate system, on which the data cutout is interpolated with the nearest-neighbor method to enable compositing across different features.

The significance of a composite field is evaluated using a two-sided Student's t test and false discovery rate (FDR; see Wilks 2006, 2016) with an α_{global} of 0.1. FDR has the advantage of

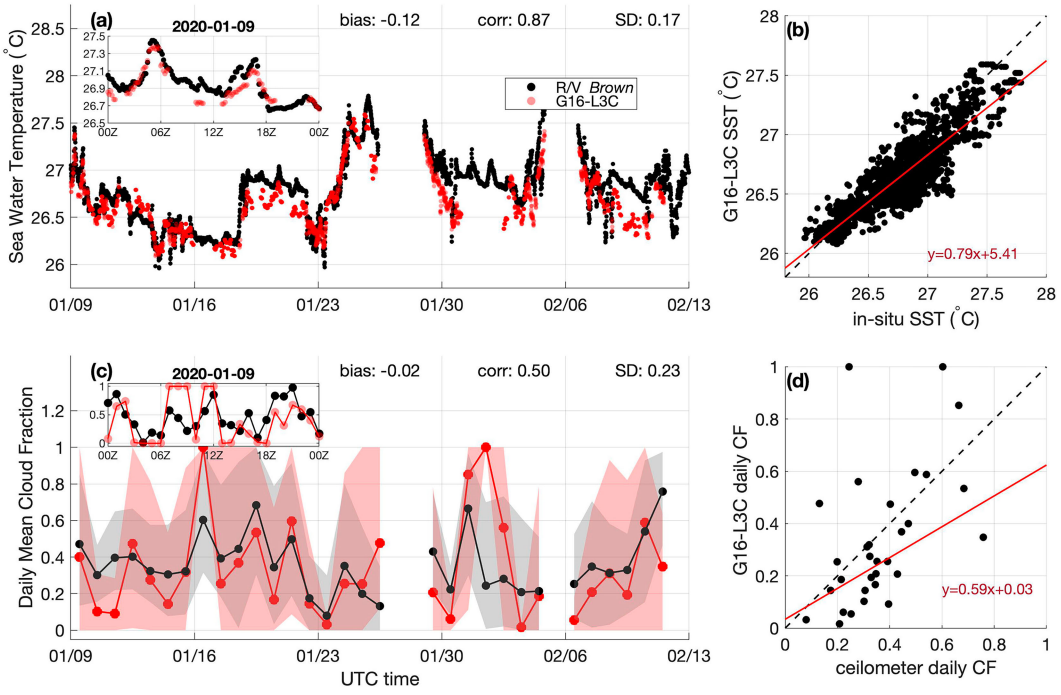

FIG. 3. Satellite data (red) compared against observations on board R/V *Brown* (black) for the entire ATOMIC period. (a),(c) Black markers represent 10-min in situ temperature measurement at 5-cm water depth and daily-mean cloud fraction computed from the hourly ceilometer cloud fraction, respectively; red markers denote the equivalent G16 L3C hourly SST retrieved in clear sky in (a) and the daily mean area cloud fraction derived from the G16 L3C SST clear-sky mask in (c). The shaded area in (c) denotes the range between 10th and 90th percentiles of hourly cloud fraction within each day. The insets in (a) and (c) show the details of SST and cloud fraction variation on 9 Jan 2020, respectively. (b),(d) Regression relation between the satellite SST and cloud fraction against in situ measurements. Black dashed line: 1-to-1 line. Red solid line: regression fit of the relation.

being conservative when the underlying data are spatially correlated (Wilks 2019). The null hypothesis (H_0) to test is that there is no coherent response pattern of a given atmospheric field to the daily SST perturbations.

4. Results

a. In situ validation of satellite SST and cloud fraction

In situ measurement of subsurface seawater temperature is used to validate the G16-L3C SST retrieval, which is one of the data sources used to generate the GPB L4 SST analysis. G16-L3C SST are well correlated (0.87) with the R/V *Brown* subsurface SST for the entire campaign period (Fig. 3a) with a −0.12-K bias and a 0.17-K standard deviation (SD) of differences. The agreement between G16-L3C SST and in situ measurements are good with the best fit line close to the 1-to-1 line (Fig. 3b). Similarly, the GPB L4 SST (not shown) has a −0.14-K bias and a 0.17-K SD. Good performance of the G16-L3C SST retrievals and the GPB L4 product relative to nighttime R/V *Brown* measurements have also been noted in Wick et al. (2023) with slightly smaller biases and 0.16-K SD. Given the favorable agreement and small diurnal SST variations throughout ATOMIC (Wick et al. 2023), the GPB L4 product is assumed to provide a reasonable estimate of the daily averaged SST field.

Daily averaged area cloud fraction derived from the G16-L3C ACSPO cloud mask along the RHB track is plotted against the ship ceilometer daily cloud fraction in Fig. 3c. Although the day-to-day variation in the satellite cloud fraction are consistent with the ceilometer observation with a 0.50 correlation, the agreement between daily averaged satellite cloud fraction and the in situ observation (Fig. 3d) is less well compared to that of the SSTs. The different field of view can be the main reason for the differences. The ceilometer footprint at cloud base is less than 10 m wide and gives the frequency of cloud detection within a given time window, while the satellite derived hourly cloud fraction is a spatial average (over 0.25° ERA5 grid) based on hourly snapshots of clear-sky detection at 2-km resolution. The cloud fraction variability within a given day, represented by the range of the central 80% of data (shaded area in Fig. 3c), tends to be larger in the satellite than in the in situ measurement.

Two examples of warm anomalies traversed by the R/V *Brown* on 9 January 2020 are zoomed in in the inset of Fig. 3a. The hourly cloud fraction measured over these two warm anomalies are also displayed in the inset of Fig. 3c. The SST space–time series shown in Fig. 3a inset consists of large-scale background SST gradients and local SST variations as R/V *Brown* headed upstream against the trade wind (Fig. 2a). The first peak of SST sampled around 0600 UTC reflects SST

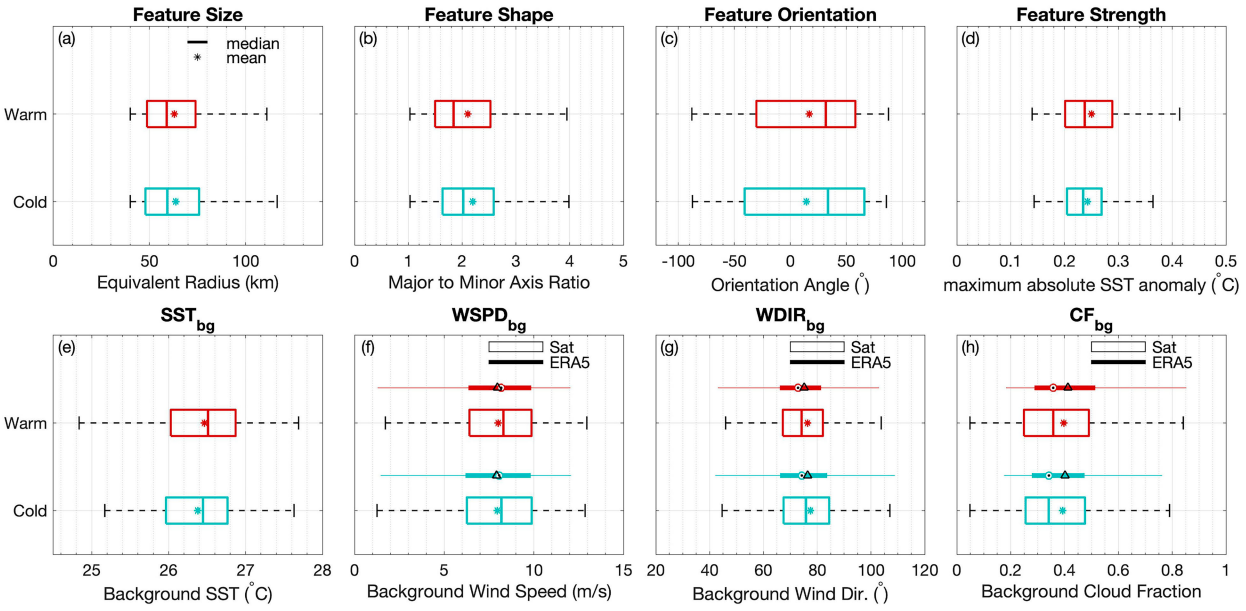

FIG. 4. Statistics of (a)–(d) characteristics and (e)–(h) background environments of warm (red) and cold (cyan) GPB SST features in the 10° × 10° study region used to construct the composite. The hollow rectangular box and filled compact box in (f)–(h) show statistics from satellite observations and ERA5, respectively. Line (target symbol) and asterisk (open black triangle) marker in the hollow (filled) rectangular box mark median and mean, respectively. The lower and upper edges of the box represent 25th and 75th percentiles, respectively. The lower and upper ends of the whiskers mark the most extreme data that are not outliers (outliers omitted) with the maximum whisker length 1.5 times the interquartile range.

variation across a linear feature detected in the G16-L3C hourly SST retrieval (indicated by dashed-gray contour in Fig. 2a) along a direction close to the minor axis of the feature. The second SST peak sampled between 1200 and 1800 UTC, however, represents the SST variation across the southern part of a large feature at a slanted angle. These two anomalies are still visible in the daily GPB SST (solid black contour in Fig. 2a), suggesting that they are persistent features on a daily time scale at the least.

Having reasonable satellite estimates of daily SST anomalies and cloud fraction is important because R/V *Brown* only sampled through about 20 SST features with different diameters and anomaly magnitudes during the entire campaign. Also, different parts of the SST features were sampled by chance at different times of the day without much consistency relative to the background wind. Hence, it is difficult to comprehensively examine the subdaily and daily SST–cloud relationship using only the ship-based measurements.

b. *Characteristics of SST features and background environments*

A subset (40%) of GPB daily SST features, whose area equivalent radius lies between 40 and 140 km (Park et al. 2006), is selected to perform composite analysis on. We summarize in Fig. 4 the characteristics of these 877 SST features and their background environments, which are representative of the full sample group (not shown), except that the subset consists of larger SST objects with stronger SST anomalies. Note that the other 60% of the SST features are mostly smaller than 40 km, where the representativeness of the in situ SST variability is reduced in L4 SST analyses (Wick et al. 2023). Including these less reliable feature locations can affect the statistical significance of the composites.

The warm and cold features share similar characteristics and background environments. Specifically, the warm and cold categories both have a mean equivalent radius R_e around 62 km (Fig. 4a), with the feature major axis length being about twice as long as the minor axis length (Fig. 4b) and mostly (>50%) oriented at more than 30° from due north (Fig. 4c). The averaged SST anomaly magnitude in both categories is about 0.25°C, with more SST warm anomalies reaching an anomaly magnitude of 0.4°C than the cold ones (Fig. 4d). The mean background SST associated with these anomalous SST features is ~26.5°C (Fig. 4e). The distribution of background wind speed and wind direction from satellite are also quite similar between the warm and cold feature groups with an 8 m s^{-1} mean wind coming from east of northeast (76°–78°) (Figs. 4f,g), indicating that the background surface wind is fairly spatially uniform as expected in the trade wind region. The ERA5 wind statistics are similar to those from CCMP-NRT. As for background mean cloudiness (Fig. 4h), both satellite and ERA5 cloud area fraction is about 0.4 over the two categories of SST anomalies. Although ERA5 represents the mean and the interquartile range of background cloud fraction reasonably well, ERA5 does not resolve cloud fraction lower than 0.2 as frequently as the satellite observation. Note that ERA5 cloud fraction is a model estimate and does not directly contain observations. The averaged decorrelation time of the SST anomalies and cloud fraction in

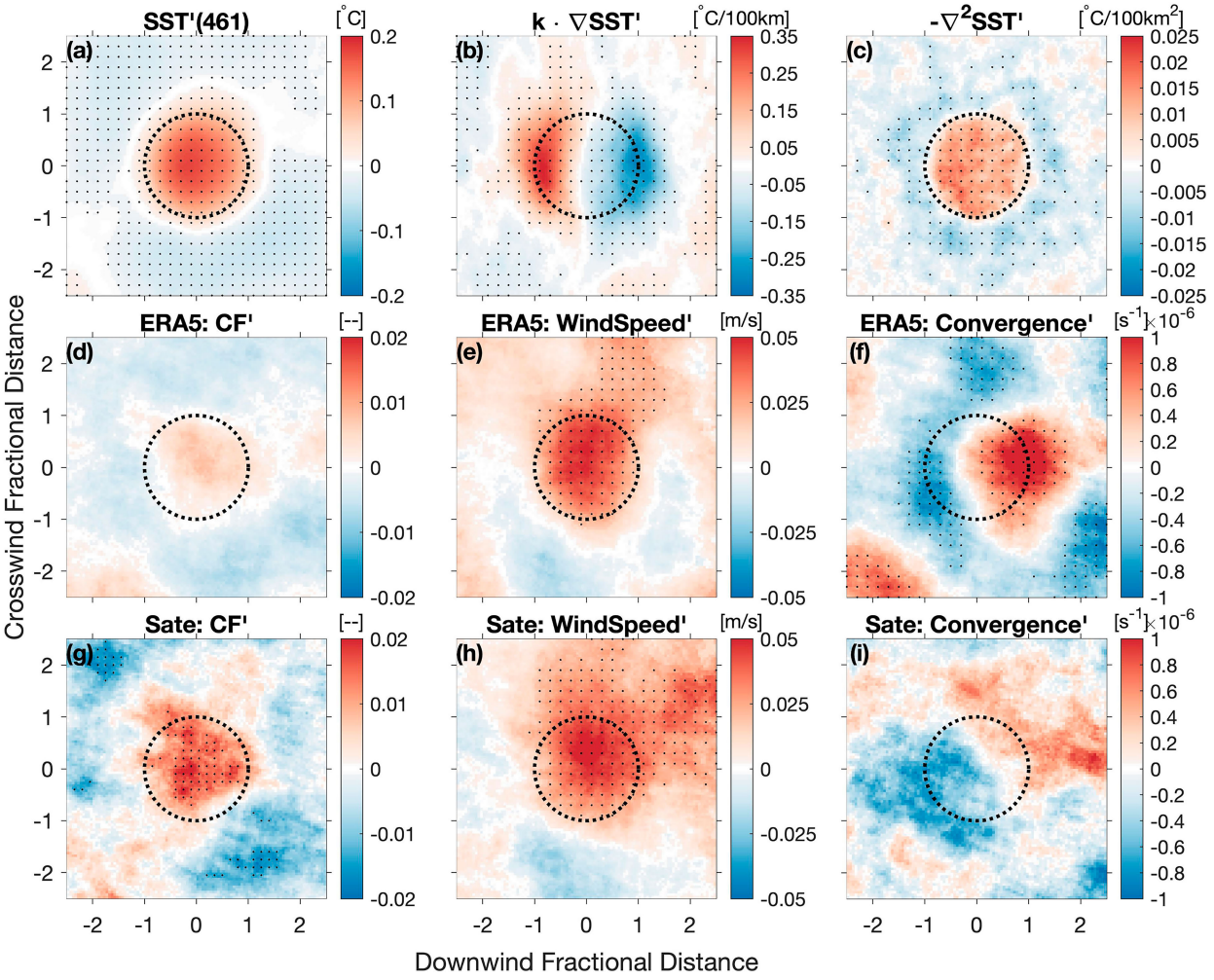

FIG. 5. Composites of various data fields over SST warm patches in a feature-centric, normalized, and wind-aligned coordinate. (a)–(c) SST warm anomalies, the downwind SST gradients, and SST Laplacian, respectively. (d)–(f) Cloudiness anomalies, wind speed magnitude anomalies, and wind convergence anomalies from ERA5 (positive = convergent), respectively. (g)–(i) As in (d)–(f), but from satellite products. X axis (Y axis) is aligned with (normal to) the direction of background mean wind. The dotted circle roughly denotes the edge of the composited warm feature. Black stippling indicates locations with 90% field significance. Note that using field significance reduces the chance of false discovery in spatially correlated data.

our study region is about 5 and 0.6 days, respectively (Fig. C1). Therefore, the SST features are still considered slow varying relative to the transient clouds.

c. *Composite response of cloudiness and 10-m surface winds to SST warm anomalies*

Composites of SST anomalies, downwind SST gradients, and SST Laplacian over 461 warm SST features are shown in Figs. 5a–c. The mean SST anomaly magnitude in the ATOMIC region is 2.5–10 times weaker than composite SST anomalies from studies of the Southern Ocean eddies (Frenger et al. 2013), Gulf Stream rings (Park et al. 2006), North Brazil Current rings (Bueno et al. 2022), and idealized eddies (Foussard et al. 2019).

Composites of ERA5 and satellite cloudiness both show an increase of cloud cover within the SST warm core (Figs. 5d,g). However, only the response in satellite composite (Fig. 5g) is statistically significant. Outside of the SST warm core, a statistically significant reduction of cloud fraction relative to the mean state is also present in the satellite composite. This signal is physical and not an artifact of our method. Note that although the cloudiness anomaly integrated over the entire study region is zero by definition, our composite method does not constrain the total cloud fraction anomalies to zero when integrated over the data cutout area. Therefore, the enhanced cloud cover over the SST warm core and reduction of cloud cover away from the SST warm core in Fig. 5g suggest that SST warm anomalies contribute to the heterogeneity of cloud fraction in nature. These satellite cloud fraction anomaly magnitudes are between 0.01 and 0.02, which is about 2%–4% of the satellite mean cloud fraction and explains 10%–15% of its small-scale (<300 km) spatial variability. The anomaly magnitude in

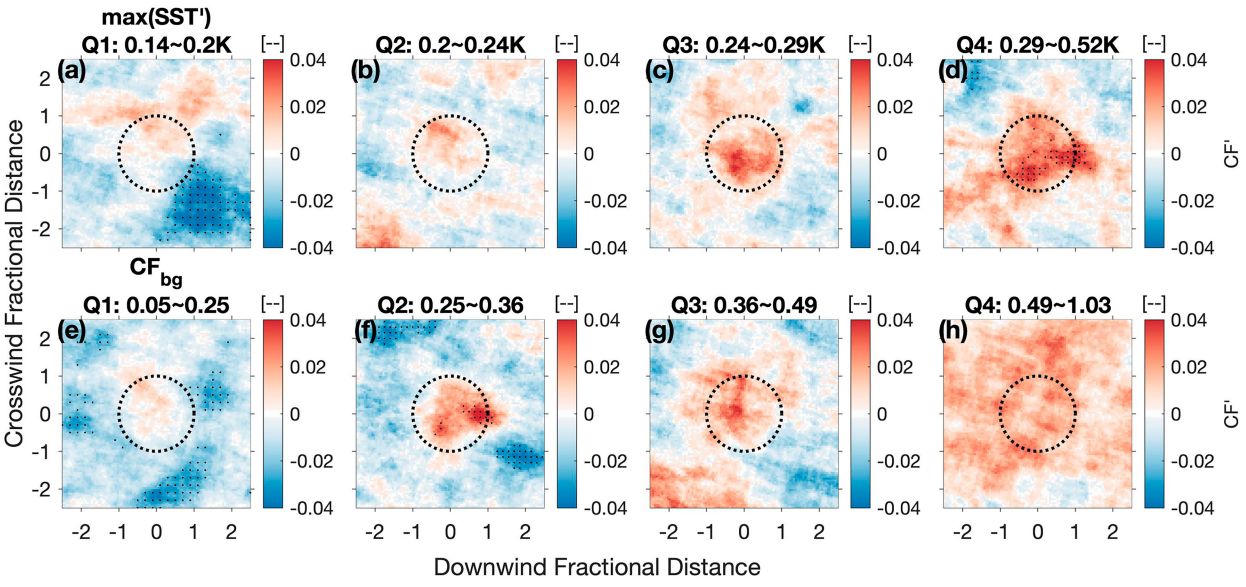

FIG. 6. Conditional composites of satellite cloud fraction anomalies in four quartiles of (a)–(d) SST warm anomaly magnitude and (e)–(h) background cloud fraction. The range of the conditioning parameter in each composite group is noted in each panel title. Plotting conventions follow Fig. 5. Note that the color bar range here is 2 times larger than that in Figs. 5d and 5g.

the ERA5 counterpart is 2 to 4 times weaker. Yet, the ERA5 cloud fraction anomalies still account for up to 10% of the high-frequency spatial variability in ERA5 cloud fraction, suggesting that the spatial variability of ERA5 cloud fraction is weaker than that in the satellite observation. The qualitatively consistent cloud response in ERA5 and satellite composites suggests that the ERA5 lower atmosphere is impacted by daily satellite SST features (from OSTIA) similar to those in the GPB product. Note, OSTIA has similar and even slightly better skill in representing subdaily in situ SST variability compared to GPB, especially in the southern part of the study region (Wick et al. 2023). Constructing the composite based on SST features detected from OSTIA (with the same criteria as GPB) gives similar cloud response results (Fig. C3).

Both ERA5 and CCMP-NRT daily averaged surface wind magnitude are increased above the SST warm anomalies by 0.05 m s^{-1} (Figs. 5e,h), which is 0.4% relative to the mean state and accounts for 8% of the small-scale (<300 km) spatial variability in 10-m wind speed in both datasets. Albeit weak in magnitude, this response is statistically significant and it is largely in phase with the SST perturbation in both products. While the wind speed anomalies look similar for both ERA5 and CCMP-NRT, the wind convergence anomalies look different (Figs. 5f,i). The ERA5 pattern resembles the Laplacian of SST, with the convergence anomaly center shifted downwind and located around the maximum SST gradient. The CCMP-NRT convergence composite appears similar to the dipole pattern of downwind SST gradients but less confined and rotated about 45° counterclockwise from the background mean wind.

Interestingly, the wind convergence anomalies are statistically significant in ERA5 but not in CCMP-NRT even though the magnitude of the anomalies in these two datasets are similar, suggesting more variability in the satellite wind convergence patterns across features. Note that we think CCMP-NRT convergence anomaly pattern is a physical signal because it remains similar over SST features that fall within the ASCAT swaths (not shown). The downwind ERA5 wind convergence anomalies reach about 60% of the background mean wind convergence and constitutes about 10% of its small-scale (<300 km) spatial variation. This is about 2 times larger than the relative magnitudes of the satellite convergence anomalies. The mechanisms associated with these wind speed and wind convergence anomaly patterns are discussed further in section 5.

The composites of cloudiness, wind speed, and wind convergence anomalies over SST cold anomalies are similar but with opposite signs (Fig. C2).

d. *Conditional composites of cloudiness anomalies over SST warm anomalies*

To better understand if the cloud response signal is stronger in certain conditions, we explore conditional composites over the 461 SST warm anomalies using different parameters. Quartiles of a given parameter are used to divide the limited samples into four more-or-less equal groups. After exhausting meaningful parameters (e.g., wind speed, inversion strength, SST anomaly size), we found that the maximum SST anomaly and background cloud fraction are the two parameters that yield further insights. Note that the magnitude of the positive cloud fraction anomaly in Fig. 5g does not show clear dependence on the large-scale lower-tropospheric stability or the estimated inversion strength. Also note that these conditional cloudiness composites shown in Fig. 6 are noisier compared to the full composite in Fig. 5 due to a smaller sample size and a large spatial variability of daily cloud fraction.

Intuitively, one may expect that stronger SST anomalies would force a larger cloudiness response. Compositing the satellite cloud fraction anomalies in the four quartiles of SST anomalies shows that the positive cloudiness anomaly over the SST warm core grows and reaches statistical significance as the magnitude of the SST warm anomalies increases (Figs. 6a–d).

Conditioning the composites by the satellite background cloud fraction, which is not correlated with the local SST anomaly magnitude, shows that the boosting effect on local cloud fraction from SST warm spots is statistically significant when the observed background cloud fraction (associated with the data cutout area) is in the second quartile between 0.25 and 0.36 (Fig. 6f). A similar signal is also discernible in the third quartile. Therefore, Figs. 6e–h suggest that the coherent signal of cloud fraction anomalies over SST warm anomalies shown in the full composite (Fig. 5g) more likely occurs when the background cloud fraction around SST warm patches are within the central 50% of the distribution than at the tails.

As SST anomaly strength or background cloud fraction increases, the composites of wind speed anomalies are positive over the SST warm core in all quartiles. But the wind speed anomaly signal does not show a similar dependence on these two parameters as the cloud fraction anomalies (not shown). The wind divergence anomalies become noisier and do not show much coherent structure over or downwind of the SST warm core (not shown). We have also tested conditional compositing using the daily area-averaged 10-m wind speed and inversion strength as in Bony et al. (2020) (see appendix C). The composite results are similar, consistently showing enhanced cloud fraction over the SST warm anomalies, yet the null hypothesis cannot be rejected (Fig. C4). A larger sample size is likely required to detect the relatively weak signal out of other spatial variability in the atmosphere.

5. Potential mechanisms linking SST anomalies to changes in surface winds and clouds

While the in-phase relationship between enhanced cloudiness (Fig. 5g) and SST warm anomalies (Fig. 5a) suggests that collocated surface convergence anomalies induced by pressure adjustment mechanism plays a dominant role in triggering cloudiness anomalies, the center of the convergence anomalies are significantly downwind from the warmest SST (Figs. 5c,f). The offset between SST anomalies and convergence makes it difficult to justify the enhanced cloudiness as a response to surface convergence and the pressure adjustment mechanism because the convergence anomalies are not collocated with SST and cloudiness anomalies. Therefore, we explore the possibility of an alternative mechanism to explain observation of increased cloudiness over warmer SST.

Cloudiness increases can be collocated with SST anomalies due to increases in boundary layer turbulence. Since turbulence is not yet measurable from satellites, its spatial variation over mesoscale SST features is often inferred from surface flux and wind speed anomalies. For example, increased turbulence over warm ocean eddies has been inferred from observations of increased 10-m surface wind speed through downward momentum transport by turbulence (Frenger et al. 2013). In a numerical model, turbulence strength can be represented by eddy diffusivity, which is a function of both the size and the kinetic energy of the turbulent eddies in the atmospheric boundary layer. In this way, Byrne et al. (2015) showed that the enhanced wind speed and cloudiness observed in Frenger et al. (2013) are associated with enhanced turbulence above warm-core ocean eddies. This phase relation also occurs over cold SST anomalies. For instance, in situ measurements show reduced cloudiness, weakened surface wind speed, and weakened vertical velocity fluctuations above an SST cold patch in the northwest tropical Atlantic (Acquistapace et al. 2022). Our in-phase relation among cloudiness anomalies, surface wind speed anomalies, and SST anomalies is consistent with the findings from these three studies.

Here, the positive cloudiness anomaly over SST warm patch can be related to cloud formation, which requires moisture and either instability or lift. Frenger et al. (2013) hypothesized that a modification of boundary layer stability in combination with changes in surface moisture supply above SST anomalies are the likely causes for enhanced cloudiness observed above Southern Ocean warm core ocean eddies. In contrast, studies of SST diurnal warming over the moist tropical Indian Ocean emphasize the lifting of moisture provided by buoyant thermals and surface driven convective turbulence (Johnson and Ciesielski 2017; de Szoeke et al. 2021). In this line of argument, the mixed-layer height surpassing the lifting condensation level (LCL) is the primary physical criterion for low-level cloud formation (Malkus 1958; Johnson and Ciesielski 2017; de Szoeke et al. 2021; Acquistapace et al. 2022).

ERA5 surface flux composites in Fig. 7 show spatial variability similar to that in the cloud fraction. Both surface sensible, latent, and buoyancy fluxes are increased over the SST warm patch and decreased in region surrounding the SST warm anomalies. This spatial variability in the ERA5 surface fluxes is qualitatively consistent with in situ observation made in ATOMIC/EUREC^{4}A region (Iyer et al. 2022a; Acquistapace et al. 2022). Hence, similar spatial variability for SST-anomaly-induced MLH variation is plausible because surface buoyancy flux is a source of subcloud-layer turbulence kinetic energy.

Interestingly, the locally increased ERA5 surface sensible and buoyancy fluxes over warmer SSTs, where surface wind is enhanced, are different from the flux response in idealized LES results in Nuijens and Stevens (2012), where surface sensible and buoyancy fluxes remained unchanged or even reduced when wind speed is uniformly increased. This may be due to the equilibrium and nonprecipitating configuration in their trade cumulus simulations. In our study period, the ERA5 background air–sea temperature difference is mainly negative (aka, air cooler than the ocean surface); hence, entrainment warming may not be strong enough to dominate other processes, such as cold-air advection, and to suppress the surface sensible and buoyancy fluxes locally. In situ observation analysis in Iyer et al. (2022a) also did not find significant spatial differences in 0.5-m air temperature between the warmer and the colder sides of an SST front. Despite this key difference, the enhanced latent heat flux associated with

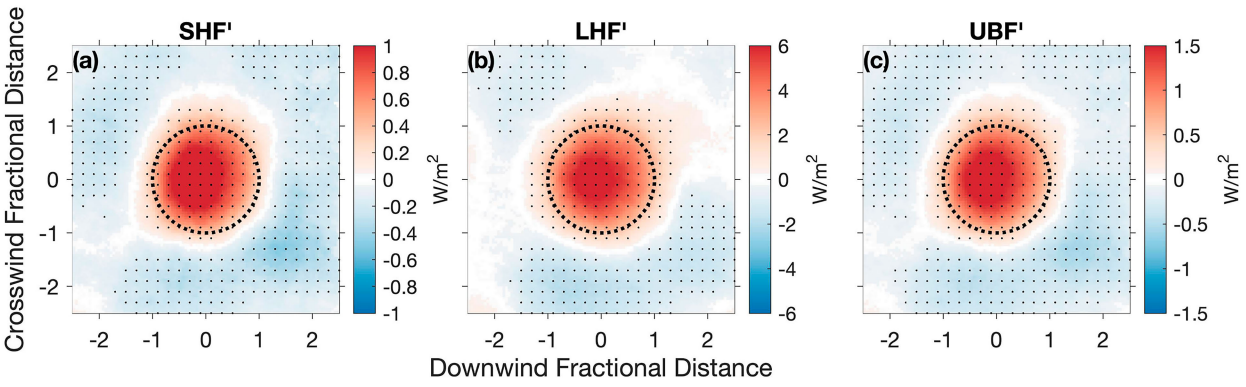

FIG. 7. Composites of ERA5 surface flux anomalies over SST warm patches. (a) Sensible heat flux anomalies, (b) latent heat flux anomalies, and (c) upward buoyancy flux anomalies. Plotting conventions follow Fig. 5.

warmer SST and enhanced surface wind speed is shared among our ERA5 composite, LES of Nuijens and Stevens (2012), and in situ observations (Johnson and Ciesielski 2017; de Szoeke et al. 2021; Iyer et al. 2022a; Acquistapace et al. 2022).

Understanding LCL response to local SST warming is challenging because it depends on small-scale temperature and moisture responses over SST warm patches. Although ERA5 estimates suggest drying and warming (hence an increased LCL) above SST warm patches (Fig. C5 in appendix C), it is unclear how reliable these ERA5 thermodynamic variables are on the scale of our interest. In addition, validating this process-level mechanism (MLH higher than LCL over warmer SSTs) with in situ observation from RHB is not a straightforward task. Only a few soundings were launched directly over SST warm and cold patches, limiting a robust statistical comparison of the behavior of LCL and MLH in different local environments. Large sample sizes are needed to average out influence from other processes that can affect the MLH relative to LCL (e.g., rain; Acquistapace et al. 2022). Also, accurately identifying 2D SST patches from the 1D ship measurements is complicated and requires some sensitivity testing. A combined process-oriented work analyzing available measurements collected in both the EUREC^{4}A and ATOMIC along with idealized LES studies might be helpful for this purpose.

6. Summary and conclusions

We have shown that submesoscale-to-mesoscale SST anomalies are ubiquitous and leave an imprint on daily mean cloud fraction in the EUREC^{4}A/ATOMIC regime, contributing to the heterogeneity or spatial variance of the cloud fraction on the daily time scale. This signal is revealed through satellite composites using 2 months of data focusing on the EUREC^{4}A/ATOMIC period. The quality of the satellite SST and cloud fraction are assessed through a comparison with the in situ observations collected on R/V *Brown*. This key finding is surprising because the spatial variability of SST over 10–100-km spatial scale is relatively weak (<0.7°C) in the tropical northwestern Atlantic trade wind alley compared to those in the tropical and extratropical boundary current regions.

Over SST warm patches, our composites show that both the daily mean cloud fraction and the 10-m surface wind speed are increased and that the sign of these modulations reverses over SST cold patches. Further, the enhancement in cloud fraction scales with the magnitude of the SST warm anomalies. The statistically significant cloud and wind speed anomalies explain up to 15% and 8% of the small-scale (<300 km) spatial variations (heterogeneity) in cloud fraction and wind speed, respectively. Interestingly, surface convergence anomalies are offset from the enhanced cloudiness and centered around the maximum downwind SST gradient. These composite results are not sensitive to the SST analysis product used.

The spatially in-phase patterns of SST, surface wind, and cloudiness anomalies favor explaining the cloud response over SST warm (cold) patches through locally enhanced (suppressed) turbulence instead of surface convergence anomalies. ERA5 composites suggest that surface sensible, latent, and buoyancy heat fluxes are also increased over SST warm anomalies, potentially increasing the mixed-layer height locally and enabling moister surface air parcel to be lifted above their LCL. These findings and interpretations are consistent with previous work in other part of the oceans (e.g., Frenger et al. 2013; Byrne et al. 2015; de Szoeke et al. 2021) and also with the in situ case studies in the same study region (Iyer et al. 2022a; Acquistapace et al. 2022).

This work suggests that thermal heterogeneity of the ocean surface represents another pathway in which mesoscale variability in clouds can arise, beyond self-aggregation due to inherent instabilities (Janssens et al. 2023) and shallow mesoscale overturning (secondary) circulations in the atmosphere (George et al. 2023). Several follow-up questions can be investigated using more years of satellite observation data and/or LES. First, does cloud response over SST anomalies depend on large-scale environmental conditions where different types of cloud organization/morphologies have been found (Bony et al. 2020)? Second, other than cloud fraction, how would the localized effect from these SST anomalies affect other aspects of the cloud (e.g., cloud-top height, morphology, or organization state; Bony et al. 2020; Luebke et al. 2022; McCoy et al. 2023), and hence affect the trade cumulus cloud radiative feedbacks? Since cloudiness

near cloud base is controlled by the local interactions of turbulent, convective, and radiative processes (Vial et al. 2017), our results imply that surface flux–turbulence–cloud interaction over mesoscale SST anomalies may be one of the important processes that needs to be better represented in climate models.

Acknowledgments. The authors thank Carl Mears, Mark Bourassa, and Jeff Whitaker for correspondence and conversations related to the CCMP wind product and ERA5 reanalysis. We also thank Gijs de Boer at NOAA Physical Sciences Laboratory, Raphaela Vogel, and two other anonymous reviewers for providing constructive feedback that improved this manuscript greatly. We acknowledge Julio Ceniceros for sharing estimations of LCL and MLH from R/V *Brown* radiosondes during revision. Discussion with Peter Blossey also contributed to this manuscript. This research is supported by NOAA Climate Program Office under Grant NOAA-OAR-CPO-2019-2005530, and in part by NOAA Cooperative Agreements NA17OAR4320101 and NA22OAR4320151. The authors appreciate additional support from NOAA Physical Sciences Laboratory. Last, the authors acknowledge scientists, technicians, and crew members who made the ATOMIC field campaign possible.

Data availability statement. ATOMIC data used in this research are accessible from https://doi.org/10.25921/etxb-ht19 and https://doi.org/10.25921/jbz6-e918. ERA5 data are obtained from the climate data store at a single level (DOI: 10.24381/cds.adbb2d47) and at pressure levels (DOI: 10.24381/cds.bd0915c6). The *GOES-16* L3C SST retrieval and the clear-sky mask can be obtained at https://doi.org/10.5067/GHG16-3UO27. GOES–POES Blended and OSTIA SST analysis are obtained from https://doi.org/10.5067/GHGPB-4FO02 and https://doi.org/10.5067/GHOST-4FK01, respectively. CCMP Near-Real-Time (NRT) version vector wind analyses are produced by Remote Sensing Systems. Data are available at www.remss.com.

APPENDIX A

Characteristics and Interpretations of SST Variations Sampled by R/V *Brown*

R/V *Brown* operated in two modes during the field campaign. On some days, it collected samples while transiting between locations. On other days, the ship stayed put at fixed locations (roughly) and measured the environments. In the former mode, the ship measured spatial–temporal variability of the SST, while in the latter mode, the ship collected time series of SST. We separated the SST records into three groups by its daily variance: weak (<25th percentile), moderate (25th–75th percentiles), and strong (>75th percentile). The daily SST variation is typically weak when R/V *Brown* stayed put, consistent with Wick et al.'s (2023) notion of weak diurnal cycle. R/V *Brown* was in transit with an average speed of 5.6 m s^{-1} on days when strong SST variations were recorded, suggesting that these SST variations are associated with spatial variability rather than temporal variability (SST anomalies hereafter).

We estimate the magnitude and size of these strong SST variations by detecting peaks and troughs in the daily R/V *Brown* SST records. The SST feature size is estimated based on the horizontal distance between the consecutive peak and trough (ΔL). The SST variation magnitude (ΔSST) is estimated as the vertical distance between the consecutive peak and trough. The associated SST spatial gradient is then estimated as $\Delta\text{SST}/\Delta L$.

The ATOMIC sampling region, away from the major western boundary currents and eddies, can be considered as the "submesoscale soup" region (Fig. 6 of McWilliams 2019). To better characterize the dynamical regimes of these SST anomalies, their Rossby number (R_o) are assessed using the cross-track component of surface current measurements via the following equation:

$$R_o = \frac{\zeta}{|f|} = \frac{\partial v}{\partial s}\Big/|f|,$$

where v is the cross-track components of the observed surface current, s is the along-track distance, and f is the Coriolis parameter. Note that estimations are made on the straight segments of the R/V *Brown* track to reflect only the changes in v.

Based on the Rossby number (not shown), the majority of the strong SST anomalies have a time scale $[1/(fR_o)]$ between 2 and 20 days, with a mean at around 6 days. Note that this time scale also supports our interpretation of these SST variations as spatial SST anomalies since the ship sampled across the associated features in less than 6 h.

APPENDIX B

Mathematical Descriptions of Coordinate Transformation

From geographical coordinates (lon, lat) to the feature-centric Cartesian coordinates (x_c, y_c),

$$\begin{aligned} x_c &= (\text{lon} - \text{lon}_0) \times r_{\text{earth}} \times \cos(\text{lat}) \\ y_c &= (\text{lat} - \text{lat}_0) \times r_{\text{earth}} \end{aligned},$$

where $(\text{lon}_0, \text{lat}_0)$ is the centroid of the detected SST anomaly; $r_{\text{earth}} = 111 \times 10^3$ m.

Rotation of coordinate is needed for several times, and it is performed by using a rotation matrix $\mathbf{M}_r(\theta)$, where θ is defined counterclockwise from the abscissas:

$$\mathbf{M}_r(\theta) = \begin{bmatrix} \cos\theta & \sin\theta \\ -\sin\theta & \cos\theta \end{bmatrix}.$$

From (x_c, y_c) to (x_n', y_n'), rotation is first performed using $\mathbf{M}_r$ to obtain (x_c', y_c'). In this step, the rotation angle θ is set as the orientation θ_o of the detected SST object:

$$\begin{bmatrix} x' \\ y' \end{bmatrix} = \mathbf{M}_r(\theta_o) \times \begin{bmatrix} x_c \\ y_c \end{bmatrix}.$$

Then, the following normalization is carried out to convert (x_c', y_c') to (x_n', y_n'):

$$x_{\text{ellp}} = \frac{ab}{\sqrt{b^2 + a^2 \tan\theta'^2}},$$

$$y_{\text{ellp}} = x_{\text{ellp}} \tan\theta',$$

$$R_n = \frac{\sqrt{x'^2 + y'^2}}{\sqrt{x_{\text{ellp}}^2 + y_{\text{ellp}}^2}},$$

where $\tan\theta' = y'/x'$;

$$(x'_n, y'_n) = R_n(\cos\theta', \sin\theta').$$

From (x'_n, y'_n) to (x''_n, y''_n), rotation is performed one more time, with the rotation angle θ as the angle between the large-scale background wind and the object orientation ($\Delta\theta_{\text{wo}}$):

$$\begin{bmatrix} x''_n \\ y''_n \end{bmatrix} = \mathbf{M}_r(\Delta\theta_{\text{wo}}) \times \begin{bmatrix} x'_n \\ y'_n \end{bmatrix}.$$

APPENDIX C

Additional Results

a. Decorrelation time scales of SST anomalies and cloud fraction

We use decorrelation time scale to estimate the life time of SST features and the spatial anomalies in cloudiness in our study region. Figure C1 supports that the cloud fields evolve much faster than the underlying SST spatial anomalies.

b. Atmospheric response over cold SST anomalies

The cold SST anomalies used for composite have similar magnitudes as its warm counterparts. The cloud fraction–surface wind speed composites from satellite and ERA5 both display similar patterns as in Fig. 5 but with opposite signs—reducing over cold SST anomalies. These atmospheric responses revealed in satellite data are qualitatively consistent with those reported over an SST cold patch in Acquistapace et al. (2022). As for surface convergence, the composite of surface convergence anomalies from CCMP-NRT shows a different dipole structure from its warm counterpart in Fig. 5i, bearing less resemblance to the downwind SST gradient dipole (Fig. C2b). Same as its warm counterpart in Fig. 5f, the ERA5 convergence anomaly pattern over SST cold patches displays a monopole pattern absent in the CCMP-NRT composite.

c. Sensitivity of composites to level-4 SST products

In the main text, composites of several atmospheric fields are constructed over SST anomalies in the GPB L4 product. Here, sensitivity of the composite results to L4 SST products is examined. Since OSTIA is assessed to be the best L4 product that captures the in situ SST variability in the ATOMIC region (Wick et al. 2023) and it is also the surface forcing used by ERA5, composites are constructed over SST anomalies in OSTIA.

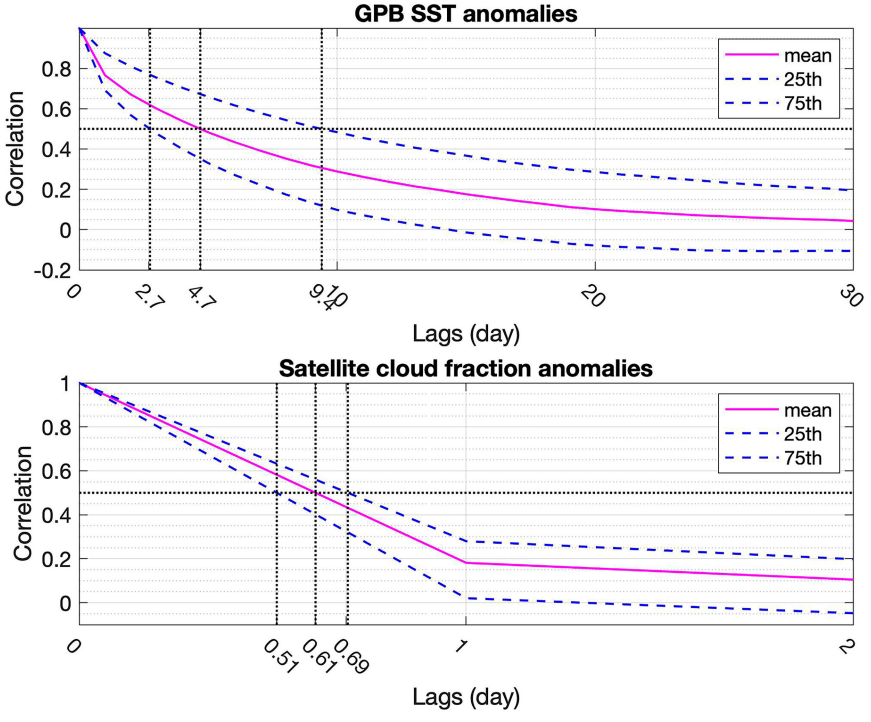

FIG. C1. Decorrelation time scale of (top) GPB SST anomalies and (bottom) satellite cloud fraction anomalies in the study region. Magenta solid lines represent the mean value. Lower and upper blue dashed lines around the magenta line mark the 25th- and 75th-percentile values.

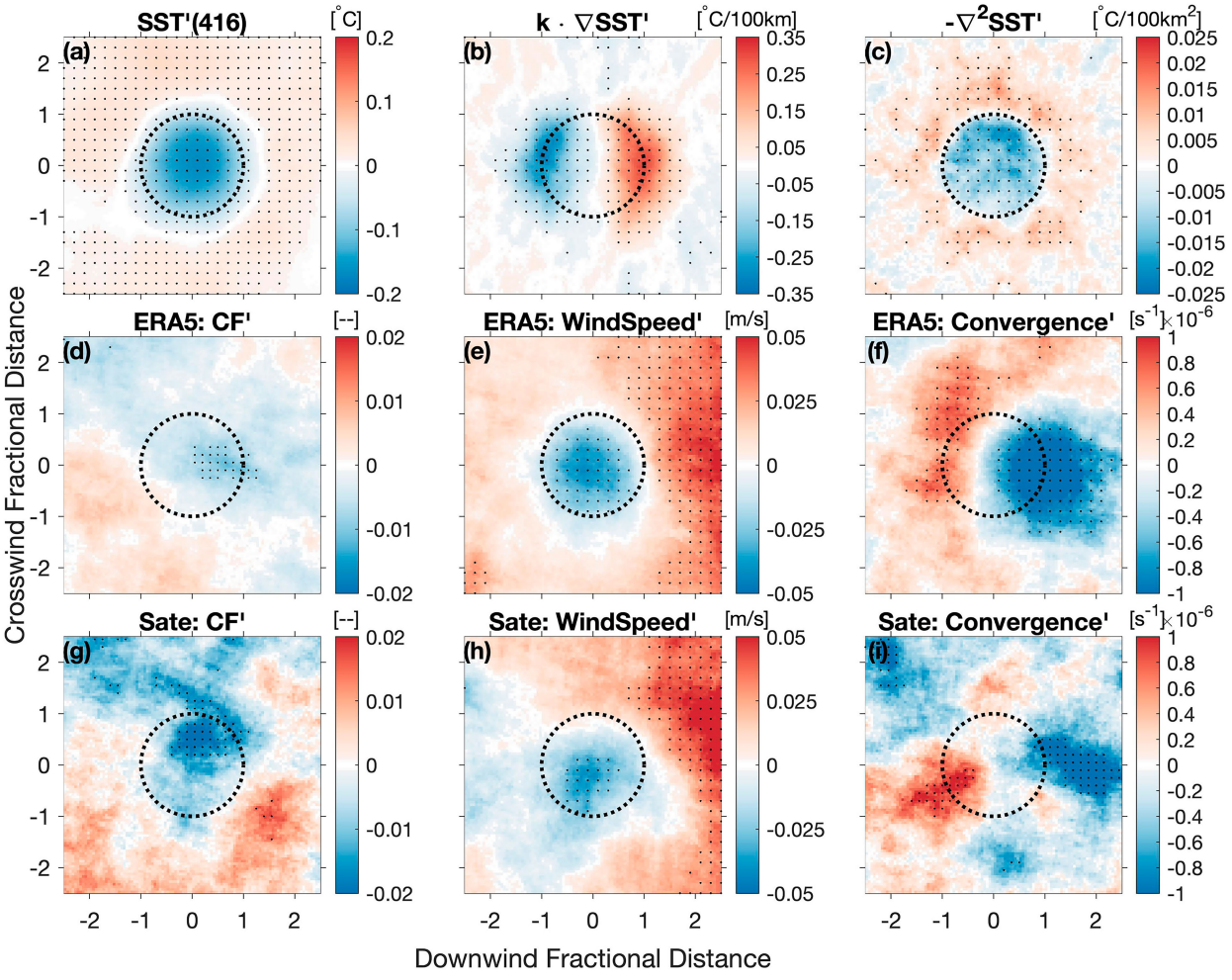

FIG. C2. As in Fig. 5, but showing composites constructed over cold anomalies in GPB.

For cloudiness anomalies, composites of satellite (Fig. C3g) and ERA5 (Fig. C3d) cloud fraction both show an increase of cloud cover within the SST warm core, similar to those in Figs. 5d and 5g. Moreover, only the response in satellite composite is statistically significant, same as that reported in the main text. Similarly, the surface wind speed is increased over SST warm core in both satellite and ERA5 composites (Figs. C3h,e). Therefore, the cloudiness and surface wind response over SST warm patches reported in the main text are robust and not dependent on the L4 SST product we use. This also holds true for responses over SST cold patches (not shown).

As for wind convergence anomalies, the composite pattern in CCMP-NRT (Fig. C3i) remains similar and insignificant as in Fig. 5i. However, the ERA5 wind convergence anomaly pattern is somewhat sensitive to the L4 SST products, showing a combination of a dipole pattern and a monopole pattern (Fig. C3f). This pattern sensitivity is likely because the ERA5 surface wind is directly forced by the OSTIA SST. Since a combined dipole and monopole pattern suggests the pressure adjustment and downward momentum mixing mechanisms acting in concert to affect surface momentum, we think that the sensitivity of the ERA5 convergence pattern to L4 SST products reflects that downward momentum mixing mechanism operates in the vicinity of SST fronts (Small et al. 2008), at a smaller spatial scale than the pressure adjustment mechanism.

d. Conditional compositing based on background environments

Recent studies have suggested that the trade cumulus cloud radiative effects depends on their organization states (Bony et al. 2020) and that the four common organization states correlate with the large-scale wind speed and inversion strength (Bony et al. 2020). Motivated by these results, we further composite the satellite observation based on the 10-m surface wind speed (U_{10}) and estimated inversion strength (EIS) using about 7.9 m s^{-1} and 0.5 K (mean values of U_{10} and EIS) as the respective threshold.

The parameter space and their conditional composites are shown in Fig. C4. First, the cloud fraction composites in different atmospheric/cloud organization regimes show

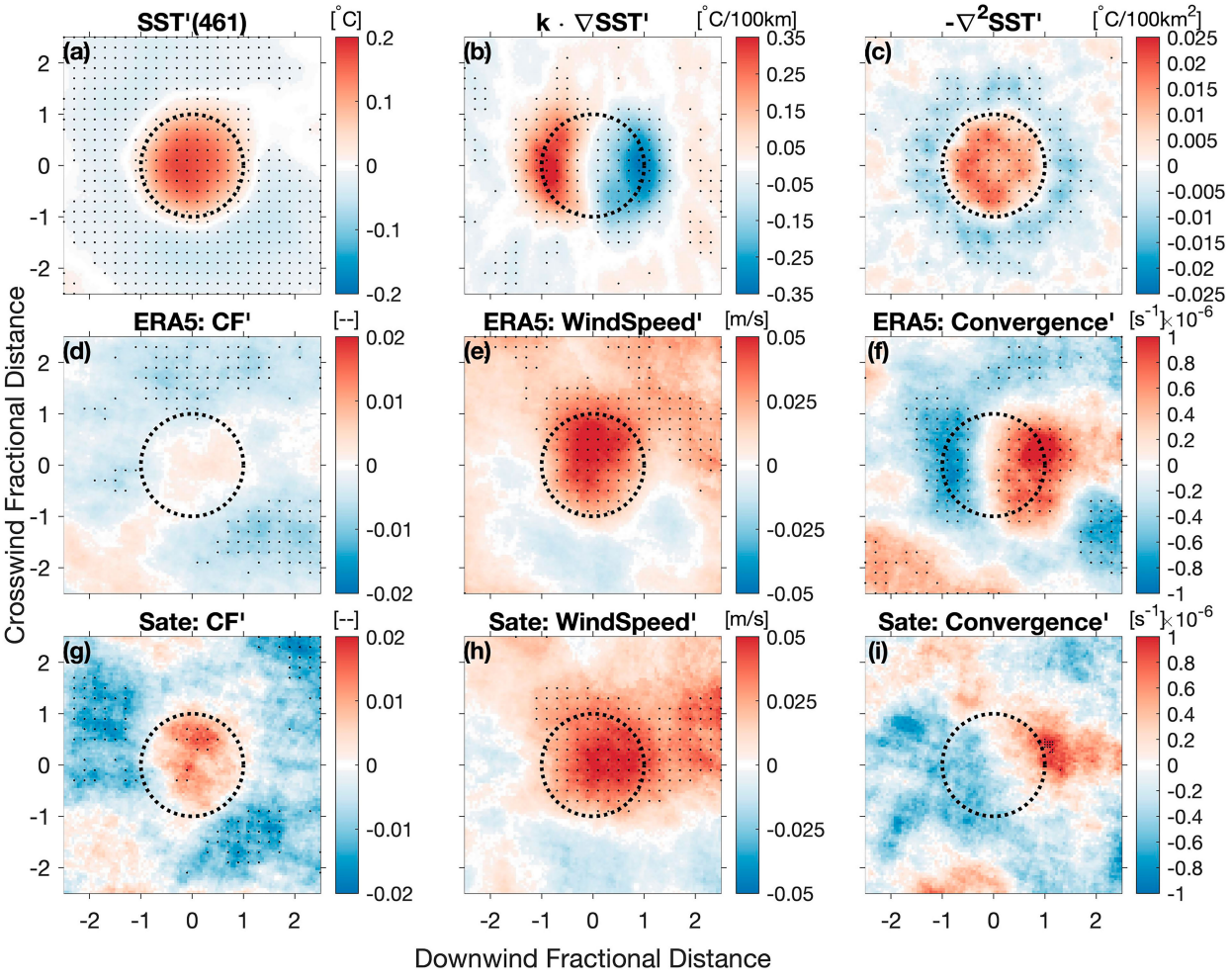

FIG. C3. As in Fig. 5, except the composites are constructed based on SST warm anomalies detected in the OSTIA SST analysis.

consistent enhancement of cloud area fraction over the SST warm anomalies, with a much weaker magnitude in the Fish-favoring regime (lower U_{10} and stronger EIS). Similarly, when the sample size is larger than 50, the increased cloud fraction over the SST warm core remains visible in different surface stability regimes. However, a lack of statistical significance of this common signal in these two independent conditional spaces suggests that the sample size here is still not large enough for us to draw any rigorous conclusions.

e. ERA5 estimated LCL and boundary layer height anomalies over SST warm patches

Daily averaged temperature and specific humidity anomalies in ERA5 suggest that air in the subcloud boundary layer is warmer and drier over SST warm patches (Figs. C5a,b), which leads to a slightly elevated LCL (Fig. C5c). The anomalies of boundary layer height (reflecting the mixed-layer height) relative to the estimated LCL are small and do not show a clear in-phase pattern with the SST warm anomalies (Fig. C5d).

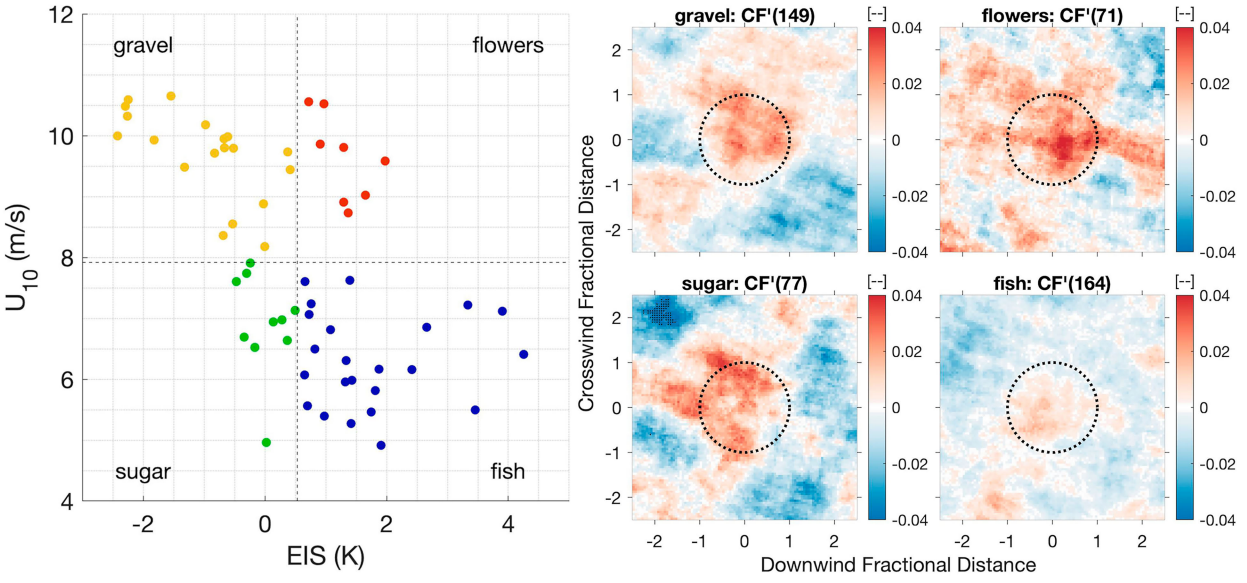

FIG. C4. Conditional composites of satellite cloud fraction anomalies in four large-scale atmospheric regimes correlated with four types of trade cumulus shallow cloud organizations (Bony et al. 2020). (left) Scatters represent the daily mean parameter values averaged over the study region (following Bony et al. 2020). Black dashed lines in both panels represent the threshold used to define the regime. (right) Composites shown follow the plotting convention in Fig. 5.

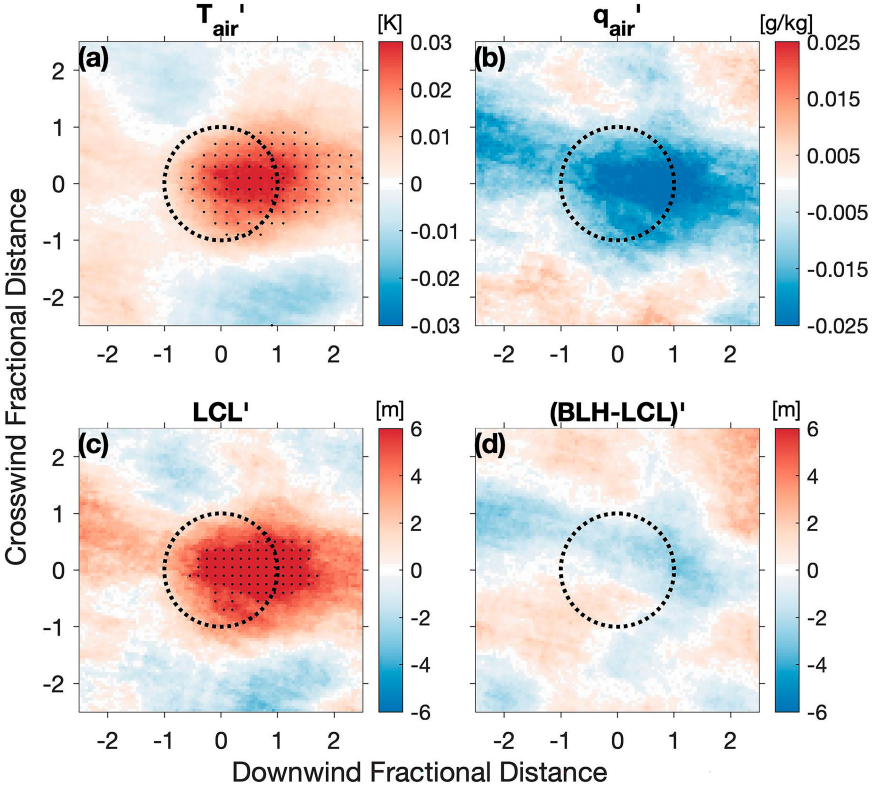

FIG. C5. Composites of 1000-hPa ERA5 (a) air temperature anomalies, (b) specific humidity anomalies, (c) LCL anomalies estimated from (a) and (b), and (d) anomalies in ERA5 boundary layer height relative to LCL over SST warm patches.

REFERENCES

Acquistapace, C., A. N. Meroni, G. Labbri, D. Lange, F. Späth, S. Abbas, and H. Bellenger, 2022: Fast atmospheric response to a cold oceanic mesoscale patch in the north-western tropical Atlantic. *J. Geophys. Res. Atmos.*, **127**, e2022JD036799, https://doi.org/10.1029/2022JD036799.

Atlas, R., R. N. Hoffman, J. Ardizzone, S. M. Leidner, J. C. Jusem, D. K. Smith, and D. Gombos, 2011: A cross-calibrated, multiplatform ocean surface wind velocity product for meteorological and oceanographic applications. *Bull. Amer. Meteor. Soc.*, **92**, 157–174, https://doi.org/10.1175/2010BAMS2946.1.

Belmonte Rivas, M., and A. Stoffelen, 2019: Characterizing ERA-Interim and ERA5 surface wind biases using ASCAT. *Ocean Sci.*, **15**, 831–852, https://doi.org/10.5194/os-15-831-2019.

Bony, S., and Coauthors, 2017: EUREC^{4}A: A field campaign to elucidate the couplings between clouds, convection and circulation. *Surv. Geophys.*, **38**, 1529–1568, https://doi.org/10.1007/s10712-017-9428-0.

——, H. Schulz, J. Vial, and B. Stevens, 2020: Sugar, gravel, fish, and flowers: Dependence of mesoscale patterns of trade-wind clouds on environmental conditions. *Geophys. Res. Lett.*, **47**, e2019GL085988, https://doi.org/10.1029/2019GL085988.

Bretherton, C. S., and P. N. Blossey, 2014: Low cloud reduction in a greenhouse-warmed climate: Results from Lagrangian LES of a subtropical marine cloudiness transition. *J. Adv. Model. Earth Syst.*, **6**, 91–114, https://doi.org/10.1002/2013MS000250.

Bueno, L. F., V. S. Costa, G. N. Mill, and A. M. Paiva, 2022: Volume and heat transports by North Brazil Current rings. *Front. Mar. Sci.*, **9**, 831098, https://doi.org/10.3389/fmars.2022.831098.

Byrne, D., L. Papritz, I. Frenger, M. Münnich, and N. Gruber, 2015: Atmospheric response to mesoscale sea surface temperature anomalies: Assessment of mechanisms and coupling strength in a high-resolution coupled model over the South Atlantic. *J. Atmos. Sci.*, **72**, 1872–1890, https://doi.org/10.1175/JAS-D-14-0195.1.

Chelton, D. B., and Coauthors, 2001: Observations of coupling between surface wind stress and sea surface temperature in the eastern tropical Pacific. *J. Climate*, **14**, 1479–1498, https://doi.org/10.1175/1520-0442(2001)014<1479:OOCBSW>2.0.CO;2.

——, M. G. Schlax, M. H. Freilich, and R. F. Milliff, 2004: Satellite measurements reveal persistent small-scale features in ocean winds. *Science*, **303**, 978–983, https://doi.org/10.1126/science.1091901.

Desbiolles, F., M. Alberti, M. E. Hamouda, A. N. Meroni, and C. Pasquero, 2021: Links between sea surface temperature structures, clouds and rainfall: Study case of the Mediterranean Sea. *Geophys. Res. Lett.*, **48**, e2020GL091839, https://doi.org/10.1029/2020GL091839.

de Szoeke, S. P., T. Marke, and W. A. Brewer, 2021: Diurnal ocean surface warming drives convective turbulence and clouds in the atmosphere. *Geophys. Res. Lett.*, **48**, e2020GL091299, https://doi.org/10.1029/2020GL091299.

Dias, J., S. N. Tulich, and G. N. Kiladis, 2012: An object-based approach to assessing the organization of tropical convection. *J. Atmos. Sci.*, **69**, 2488–2504, https://doi.org/10.1175/JAS-D-11-0293.1.

Foussard, A., G. Lapeyre, and R. Plougonven, 2019: Response of surface wind divergence to mesoscale SST anomalies under different wind conditions. *J. Atmos. Sci.*, **76**, 2065–2082, https://doi.org/10.1175/JAS-D-18-0204.1.

Fratantoni, D. M., and D. A. Glickson, 2002: North Brazil Current ring generation and evolution observed with SeaWiFS. *J. Phys. Oceanogr.*, **32**, 1058–1074, https://doi.org/10.1175/1520-0485(2002)032<1058:NBCRGA>2.0.CO;2.

——, and P. L. Richardson, 2006: The evolution and demise of North Brazil Current rings. *J. Phys. Oceanogr.*, **36**, 1241–1264, https://doi.org/10.1175/JPO2907.1.

Frenger, I., N. Gruber, R. Knutti, and M. Münnich, 2013: Imprint of Southern Ocean eddies on winds, clouds and rainfall. *Nat. Geosci.*, **6**, 608–612, https://doi.org/10.1038/ngeo1863.

George, G., B. Stevens, S. Bony, R. Vogel, and A. K. Naumann, 2023: Widespread shallow mesoscale circulations observed in the trades. *Nat. Geosci.*, **16**, 584–589, https://doi.org/10.1038/s41561-023-01215-1.

Good, S., and Coauthors, 2020: The current configuration of the OSTIA system for operational production of foundation sea surface temperature and ice concentration analyses. *Remote Sens.*, **12**, 720, https://doi.org/10.3390/rs12040720.

Hayes, S. P., M. J. McPhaden, and J. M. Wallace, 1989: The influence of sea-surface temperature on surface wind in the eastern equatorial Pacific: Weekly to monthly variability. *J. Climate*, **2**, 1500–1506, https://doi.org/10.1175/1520-0442(1989)002<1500:TIOSST>2.0.CO;2.

Heidinger, A., and W. Straka, 2020: NOAA Enterprise Cloud Mask. NOAA NESDIS STAR Algorithm Theoretical Basis Doc., version 1.2, 73 pp., https://www.star.nesdis.noaa.gov/jpss/documents/ATBD/ATBD_EPS_Cloud_Mask_v1.2.pdf.

Hersbach, H., and Coauthors, 2020: The ERA5 global reanalysis. *Quart. J. Roy. Meteor. Soc.*, **146**, 1999–2049, https://doi.org/10.1002/qj.3803.

Iyer, S., K. Drushka, E. J. Thompson, and J. Thomson, 2022a: Small-scale spatial variations of air-sea heat, moisture, and buoyancy fluxes in the tropical trade winds. *J. Geophys. Res. Oceans*, **127**, e2022JC018972, https://doi.org/10.1029/2022JC018972.

——, J. Thomson, E. Thompson, and K. Drushka, 2022b: Variations in wave slope and momentum flux from wave-current interactions in the tropical trade winds. *J. Geophys. Res. Oceans*, **127**, e2021JC018003, https://doi.org/10.1029/2021JC018003.

Janssens, M., J. V.-G. de Arellano, C. C. van Heerwaarden, S. R. de Roode, A. P. Siebesma, and F. Glassmeier, 2023: Nonprecipitating shallow cumulus convection is intrinsically unstable to length scale growth. *J. Atmos. Sci.*, **80**, 849–870, https://doi.org/10.1175/JAS-D-22-0111.1.

Johnson, R. H., and P. E. Ciesielski, 2017: Multiscale variability of the atmospheric boundary layer during DYNAMO. *J. Atmos. Sci.*, **74**, 4003–4021, https://doi.org/10.1175/JAS-D-17-0182.1.

King, G. P., M. Portabella, W. Lin, and A. Stoffelen, 2022: Correlating extremes in wind divergence with extremes in rain over the tropical Atlantic. *Remote Sens.*, **14**, 1147, https://doi.org/10.3390/rs14051147.

Klein, S. A., A. Hall, J. R. Norris, and R. Pincus, 2017: Low-cloud feedbacks from cloud-controlling factors: A review. *Surv. Geophys.*, **38**, 1307–1329, https://doi.org/10.1007/s10712-017-9433-3.

Kruse, C. G., and R. B. Smith, 2015: Gravity wave diagnostics and characteristics in mesoscale fields. *J. Atmos. Sci.*, **72**, 4372–4392, https://doi.org/10.1175/JAS-D-15-0079.1.

Lambaerts, J., G. Lapeyre, R. Plougonven, and P. Klein, 2013: Atmospheric response to sea surface temperature mesoscale structures. *J. Geophys. Res. Atmos.*, **118**, 9611–9621, https://doi.org/10.1002/jgrd.50769.

Li, Y., and R. E. Carbone, 2012: Excitation of rainfall over the tropical western Pacific. *J. Atmos. Sci.*, **69**, 2983–2994, https://doi.org/10.1175/JAS-D-11-0245.1.

Lindzen, R. S., and S. Nigam, 1987: On the role of sea surface temperature gradients in forcing low-level winds and convergence in the tropics. *J. Atmos. Sci.*, **44**, 2418–2436, https://doi.org/10.1175/1520-0469(1987)044<2418:OTROSS>2.0.CO;2.

Luebke, A. E., A. Ehrlich, M. Schäfer, K. Wolf, and M. Wendisch, 2022: An assessment of macrophysical and microphysical cloud properties driving radiative forcing of shallow trade-wind clouds. *Atmos. Chem. Phys.*, **22**, 2727–2744, https://doi.org/10.5194/acp-22-2727-2022.

Malkus, J. S., 1957: Trade cumulus cloud groups: Some observations suggesting a mechanism of their origin. *Tellus*, **9**, 33–44, https://doi.org/10.1111/j.2153-3490.1957.tb01851.x.

——, 1958: On the structure of the trade wind moist layer. MIT and WHOI Papers in Physical Oceanography and Meteorology, Vol. 13, No. 2, 47 pp.

Maturi, E., A. Harris, J. Mittaz, J. Sapper, G. Wick, X. Zhu, P. Dash, and P. Koner, 2017: A new high-resolution sea surface temperature blended analysis. *Bull. Amer. Meteor. Soc.*, **98**, 1015–1026, https://doi.org/10.1175/BAMS-D-15-00002.1.

Mauzole, Y. L., 2022: Objective delineation of persistent SST fronts based on global satellite observations. *Remote Sens. Environ.*, **269**, 112798, https://doi.org/10.1016/j.rse.2021.112798.

McCoy, D. T., R. Eastman, D. L. Hartmann, and R. Wood, 2017: The change in low cloud cover in a warmed climate inferred from AIRS, MODIS, and ERA-Interim. *J. Climate*, **30**, 3609–3620, https://doi.org/10.1175/JCLI-D-15-0734.1.

McCoy, I. L., D. T. McCoy, R. Wood, P. Zuidema, and F. A.-M. Bender, 2023: The role of mesoscale cloud morphology in the shortwave cloud feedback. *Geophys. Res. Lett.*, **50**, e2022GL101042, https://doi.org/10.1029/2022GL101042.

McWilliams, J. C., 2019: A survey of submesoscale currents. *Geosci. Lett.*, **6**, 3, https://doi.org/10.1186/s40562-019-0133-3.

Mears, C. A., J. Scott, F. J. Wentz, L. Ricciardulli, S. M. Leidner, R. Hoffman, and R. Atlas, 2019: A near-real-time version of the Cross-Calibrated Multiplatform (CCMP) ocean surface wind velocity data set. *J. Geophys. Res. Oceans*, **124**, 6997–7010, https://doi.org/10.1029/2019JC015367.

Meroni, A. N., M. Giurato, F. Ragone, and C. Pasquero, 2020: Observational evidence of the preferential occurrence of wind convergence over sea surface temperature fronts in the Mediterranean. *Quart. J. Roy. Meteor. Soc.*, **146**, 1443–1458, https://doi.org/10.1002/qj.3745.

Minobe, S., A. Kuwano-Yoshida, N. Komori, S.-P. Xie, and R. J. Small, 2008: Influence of the Gulf Stream on the troposphere. *Nature*, **452**, 206–209, https://doi.org/10.1038/nature06690.

Nuijens, L., and B. Stevens, 2012: The influence of wind speed on shallow marine cumulus convection. *J. Atmos. Sci.*, **69**, 168–184, https://doi.org/10.1175/JAS-D-11-02.1.

O'Neill, L. W., D. B. Chelton, and S. K. Esbensen, 2003: Observations of SST-induced perturbations of the wind stress field over the Southern Ocean on seasonal timescales. *J. Climate*, **16**, 2340–2354, https://doi.org/10.1175/2780.1.

——, ——, ——, and F. J. Wentz, 2005: High-resolution satellite measurements of the atmospheric boundary layer response to SST variations along the Agulhas Return Current. *J. Climate*, **18**, 2706–2723, https://doi.org/10.1175/JCLI3415.1.

——, ——, and ——, 2010a: The effects of SST-induced surface wind speed and direction gradients on midlatitude surface vorticity and divergence. *J. Climate*, **23**, 255–281, https://doi.org/10.1175/2009JCLI2613.1.

——, S. K. Esbensen, N. Thum, R. M. Samelson, and D. B. Chelton, 2010b: Dynamical analysis of the boundary layer and surface wind responses to mesoscale SST perturbations. *J. Climate*, **23**, 559–581, https://doi.org/10.1175/2009JCLI2662.1.

Park, K. A., P. Cornillon, and D. L. Codiga, 2006: Modification of surface winds near ocean fronts: Effects of Gulf Stream rings on scatterometer (QuikSCAT, NSCAT) wind observations. *J. Geophys. Res.*, **111**, C03021, https://doi.org/10.1029/2005JC003016.

Petrenko, B., A. Ignatov, Y. Kihai, and A. Heidinger, 2010: Clear-sky mask for the Advanced Clear-Sky Processor for Oceans. *J. Atmos. Oceanic Technol.*, **27**, 1609–1623, https://doi.org/10.1175/2010JTECHA1413.1.

——, ——, ——, and M. Pennybacker, 2019: Optimization of sensitivity of GOES-16 ABI sea surface temperature by matching satellite observations with L4 analysis. *Remote Sens.*, **11**, 206, https://doi.org/10.3390/rs11020206.

Quinn, P. K., and Coauthors, 2021: Measurements from the RV *Ronald H. Brown* and related platforms as part of the Atlantic Tradewind Ocean-Atmosphere Mesoscale Interaction Campaign (atomic). *Earth Syst. Sci. Data*, **13**, 1759–1790, https://doi.org/10.5194/essd-13-1759-2021.

Rieck, M., L. Nuijens, and B. Stevens, 2012: Marine boundary layer cloud feedbacks in a constant relative humidity atmosphere. *J. Atmos. Sci.*, **69**, 2538–2550, https://doi.org/10.1175/JAS-D-11-0203.1.

Savazzi, A. C. M., L. Nuijens, I. Sandu, G. George, and P. Bechtold, 2022: The representation of the trade winds in ECMWF forecasts and reanalyses during EUREC^{4}A. *Atmos. Chem. Phys.*, **22**, 13 049–13 066, https://doi.org/10.5194/acp-22-13049-2022.

Schneider, N., and B. Qiu, 2015: The atmospheric response to weak sea surface temperature fronts. *J. Atmos. Sci.*, **72**, 3356–3377, https://doi.org/10.1175/JAS-D-14-0212.1.

Schulz, H., R. Eastman, and B. Stevens, 2021: Characterization and evolution of organized shallow convection in the downstream North Atlantic trades. *J. Geophys. Res. Atmos.*, **126**, e2021JD034575, https://doi.org/10.1029/2021JD034575.

Scott, R. C., T. A. Myers, J. R. Norris, M. D. Zelinka, S. A. Klein, M. Sun, and D. R. Doelling, 2020: Observed sensitivity of low-cloud radiative effects to meteorological perturbations over the global oceans. *J. Climate*, **33**, 7717–7734, https://doi.org/10.1175/JCLI-D-19-1028.1.

Seo, H., and Coauthors, 2023: Ocean mesoscale and frontal-scale ocean–atmosphere interactions and influence on large-scale climate: A review. *J. Climate*, **36**, 1981–2013, https://doi.org/10.1175/JCLI-D-21-0982.1.

Shimada, T., and S. Minobe, 2011: Global analysis of the pressure adjustment mechanism over sea surface temperature fronts using AIRS/Aqua data. *Geophys. Res. Lett.*, **38**, L06704, https://doi.org/10.1029/2010GL046625.

Skyllingstad, E. D., S. P. de Szoeke, and L. W. O'Neill, 2019: Modeling the transient response of tropical convection to mesoscale SST variations. *J. Atmos. Sci.*, **76**, 1227–1244, https://doi.org/10.1175/JAS-D-18-0079.1.

Small, R. J., and Coauthors, 2008: Air–sea interaction over ocean fronts and eddies. *Dyn. Atmos. Oceans*, **45**, 274–319, https://doi.org/10.1016/j.dynatmoce.2008.01.001.

Spall, M. A., 2007: Midlatitude wind stress–sea surface temperature coupling in the vicinity of oceanic fronts. *J. Climate*, **20**, 3785–3801, https://doi.org/10.1175/JCLI4234.1.

Stevens, B., and Coauthors, 2021: EUREC^{4}A. *Earth Syst. Sci. Data*, **13**, 4067–4119, https://doi.org/10.5194/essd-13-4067-2021.

Thompson, E., C. Fairall, S. Pezoa, and L. Bariteau, 2021a: ATOMIC ship ceilometer: Cloud base height and vertical profiles of visible light backscattered from aerosols and clouds in the atmospheric boundary layer estimated from a vertically-

pointing lidar remote sensing instrument aboard NOAA ship Ronald H. Brown in the North Atlantic Ocean, near Barbados: Atlantic Tradewind Ocean-Atmosphere Mesoscale Interaction Campaign 2010-01-09 to 2010-02-12. NOAA NCEI, accessed February 2022, https://doi.org/10.25921/jbz6-e918.

——, ——, ——, and ——, 2021b: ATOMIC ship navigation, meteorology, seawater, fluxes: Near-surface meteorology, air-sea fluxes, surface ocean waves, and near surface ocean parameters (temperature, salinity, currents) and primary dataset of ship location and navigation estimated from in-situ and remote sensing instruments aboard NOAA ship Ronald H. Brown in the North Atlantic Ocean, near Barbados: Atlantic Tradewind Ocean-Atmosphere Mesoscale Interaction Campaign 2020-01-09 to 2020-02-12. NOAA NCEI, accessed August 2021, https://doi.org/10.25921/etxb-ht19.

Vial, J., S. Bony, B. Stevens, and R. Vogel, 2017: Mechanisms and model diversity of trade-wind shallow cumulus cloud feedbacks: A review. *Surv. Geophys.*, **38**, 1331–1353, https://doi.org/10.1007/s10712-017-9418-2.

Vogel, R., A. L. Albright, J. Vial, G. George, B. Stevens, and S. Bony, 2022: Strong cloud–circulation coupling explains weak trade cumulus feedback. *Nature*, **612**, 696–700, https://doi.org/10.1038/s41586-022-05364-y.

Wallace, J. M., T. P. Mitchell, and C. Deser, 1989: The influence of sea-surface temperature on surface wind in the eastern equatorial Pacific: Seasonal and interannual variability. *J. Climate*, **2**, 1492–1499, https://doi.org/10.1175/1520-0442(1989)002<1492:TIOSST>2.0.CO;2.

Wick, G. A., D. L. Jackson, and S. L. Castro, 2023: Assessing the ability of satellite sea surface temperature analyses to resolve spatial variability—The northwest tropical Atlantic ATOMIC region. *Remote Sens. Environ.*, **284**, 113377, https://doi.org/10.1016/j.rse.2022.113377.

Wilks, D. S., 2006: On "field significance" and the false discovery rate. *J. Appl. Meteor. Climatol.*, **45**, 1181–1189, https://doi.org/10.1175/JAM2404.1.

——, 2016: "The stippling shows statistically significant grid points": How research results are routinely overstated and overinterpreted, and what to do about it. *Bull. Amer. Meteor. Soc.*, **97**, 2263–2273, https://doi.org/10.1175/BAMS-D-15-00267.1.

——, 2019: Frequentist statistical inference. *Statistical Methods in the Atmospheric Sciences*, 4th ed. D. S. Wilks, Ed., Elsevier, 143–207, https://doi.org/10.1016/B978-0-12-815823-4.00005-5.